

TOI-954 b and EPIC 246193072 b: Short-Period Saturn-Mass Planets that Test Whether Irradiation Leads to Inflation

LIZHOU SHA,¹ CHELSEA X. HUANG,^{1,*} AVI SHPORER,¹ JOSEPH E. RODRIGUEZ,² ANDREW VANDERBURG,^{3,†} RAFAEL BRAHM,^{4,5}
JANIS HAGELBERG,^{6,‡} ELISABETH C. MATTHEWS,¹ CARL ZIEGLER,⁷ JOHN H. LIVINGSTON,⁸ KEIVAN G. STASSUN,⁹
DUNCAN J. WRIGHT,¹⁰ JEFFREY D. CRANE,¹¹ NÉSTOR ESPINOZA,¹² FRANÇOIS BOUCHY,⁶ GÁSPÁR Á. BAKOS,^{13,14,§}
KAREN A. COLLINS,² GEORGE ZHOU,² ALLYSON BIERYLA,² JOEL D. HARTMAN,¹³ ROBERT A. WITTENMYER,¹⁰
LOUISE D. NIELSEN,⁶ PETER PLAVCHAN,¹⁵ DANIEL BAYLISS,¹⁶ PAULA SARKIS,¹⁷ THIAM-GUAN TAN,¹⁸ RYAN CLOUTIER,²
LUIGI MANCINI,^{19,17,20} ANDRÉS JORDÁN,^{4,5} SHARON WANG,¹¹ THOMAS HENNING,¹⁷ NORIO NARITA,^{21,22,23,24,25}
KALOYAN PENEV,²⁶ JOHANNA K. TESKE,^{11,¶} STEPHEN R. KANE,²⁷ ANDREW W. MANN,²⁸ BRETT C. ADDISON,¹⁰
MOTOHIDE TAMURA,^{8,23,24} JONATHAN HORNER,¹⁰ MAURO BARBIERI,²⁹ JENNIFER A. BURT,³⁰ MATÍAS R. DÍAZ,³¹
IAN J. M. CROSSFIELD,^{32,1} DIANA DRAGOMIR,³³ HOLGER DRASS,³⁴ ADINA D. FEINSTEIN,^{35,**} HUI ZHANG,³⁶ RHODES HART,³⁷
JOHN F. KIELKOPF,³⁸ ERIC L. N. JENSEN,³⁹ BENJAMIN T. MONTET,⁴⁰ GAËL OTTONI,⁶ RICHARD P. SCHWARZ,⁴¹ FELIPE ROJAS,^{42,5}
DAVID LOPEZ FDEZ NESPRAL,^{43,44} PASCAL TORRES,⁴² MATTHEW W. MENGEL,¹⁰ STÉPHANE UDRY,⁶ ABNER ZAPATA,³⁴
ERIN SNODDY,³⁹ JACK OKUMURA,¹⁰ GEORGE R. RICKER,¹ ROLAND K. VANDERSPEK,¹ DAVID W. LATHAM,² JOSHUA N. WINN,⁴⁵
SARA SEAGER,^{1,46,47} JON M. JENKINS,⁴⁸ KNICOLE D. COLÓN,⁴⁹ CHRISTOPHER E. HENZE,⁴⁸ AKSHATA KRISHNAMURTHY,¹
ERIC B. TING,⁴⁸ MICHAEL VEZIE,¹ AND STEVEN VILLANUEVA,^{1,††}

¹*Department of Physics and Kavli Institute for Astrophysics and Space Research,
Massachusetts Institute of Technology, 77 Massachusetts Ave, Cambridge, MA 02139, USA*

²*Center for Astrophysics | Harvard & Smithsonian, 60 Garden Street, Cambridge, MA 02138, USA*

³*Department of Astronomy, The University of Texas at Austin, Austin, TX 78705, USA*

⁴*Facultad de Ingeniería y Ciencias, Universidad Adolfo Ibáñez, Av.Diagonal las Torres 2640, Peñalolén, Santiago, Chile*

⁵*Millennium Institute for Astrophysics, Chile*

⁶*Geneva Observatory, University of Geneva, Chemin des Maillettes 51, 1290 Versoix, Switzerland*

⁷*Dunlap Institute for Astronomy and Astrophysics, University of Toronto, 50 St. George Street, Toronto, Ontario M5S 3H4, Canada*

⁸*Department of Astronomy, University of Tokyo, 7-3-1 Hongo, Bunkyo-ku, Tokyo 113-0033, Japan*

⁹*Department of Physics & Astronomy, Vanderbilt University, Nashville, TN 37235, USA*

¹⁰*University of Southern Queensland, Centre for Astrophysics, West Street, Toowoomba, QLD 4350 Australia*

¹¹*The Observatories of the Carnegie Institution for Science, 813 Santa Barbara Street, Pasadena, CA, 91101, USA*

¹²*Space Telescope Science Institute, 3700 San Martin Drive, Baltimore, MD 21218, USA*

¹³*Department of Astrophysical Sciences, Princeton University, NJ 08544, USA*

¹⁴*MTA Distinguished Guest Fellow, Konkoly Observatory, Hungary*

¹⁵*George Mason University, 4400 University Drive MS 3F3, Fairfax, VA 22030, USA*

¹⁶*Department of Physics, University of Warwick, Gibbet Hill Road, Coventry CV4 7AL, UK*

¹⁷*Max-Planck-Institut für Astronomie, Königstuhl 17, Heidelberg 69117, Germany*

¹⁸*Perth Exoplanet Survey Telescope, Perth, Australia*

¹⁹*Department of Physics, University of Rome “Tor Vergata”, Via della Ricerca Scientifica 1, Roma I-00133, Italy*

²⁰*INAF – Astrophysical Observatory of Turin, Via Osservatorio 20, Pino Torinese I-10025, Italy*

²¹*Komaba Institute for Science, The University of Tokyo, 3-8-1 Komaba, Meguro, Tokyo 153-8902, Japan*

²²*JST, PRESTO, 3-8-1 Komaba, Meguro, Tokyo 153-8902, Japan*

²³*Astrobiology Center, 2-21-1 Osawa, Mitaka, Tokyo 181-8588, Japan*

²⁴*National Astronomical Observatory of Japan, 2-21-1 Osawa, Mitaka, Tokyo 181-8588, Japan*

²⁵*Instituto de Astrofísica de Canarias (IAC), 38205 La Laguna, Tenerife, Spain*

²⁶*Department of Physics, University of Texas at Dallas, Richardson, TX 75080, USA*

²⁷*Department of Earth and Planetary Sciences, University of California, Riverside, CA 92521, USA*

²⁸*Department of Physics and Astronomy, The University of North Carolina at Chapel Hill, Chapel Hill, NC 27599-3255, USA*

²⁹*INCT, Universidad de Atacama, Calle Copayapu 485, Copiapó, Atacama, Chile*

³⁰*Jet Propulsion Laboratory, California Institute of Technology, 4800 Oak Grove Drive, Pasadena, CA 91109, USA*

³¹*Departamento de Astronomía, Universidad de Chile, Camino El Observatorio 1515, Las Condes, Santiago, Chile*

³²*Department of Physics and Astronomy, University of Kansas, 1251 Wescoe Hall Dr., Lawrence, KS 66045, USA*

³³*Department of Physics and Astronomy, University of New Mexico, 1919 Lomas Blvd NE, Albuquerque, NM 87131, USA*

³⁴Center of Astro-Engineering UC, Pontificia Universidad Católica de Chile, Av. Vicuña Mackenna 4860, Macul, Santiago, Chile

³⁵Department of Astronomy and Astrophysics, University of Chicago, 5640 S. Ellis Ave, Chicago, IL 60637, USA

³⁶School of Astronomy and Space Science, Key Laboratory of Modern Astronomy and Astrophysics in Ministry of Education, Nanjing University, Nanjing 210046, Jiangsu, China

³⁷Centre for Astrophysics, University of Southern Queensland, Toowoomba, QLD, 4350, Australia

³⁸Department of Physics and Astronomy, University of Louisville, Louisville, KY 40292, USA

³⁹Department of Physics & Astronomy, Swarthmore College, Swarthmore PA 19081, USA

⁴⁰School of Physics, University of New South Wales, Sydney, NSW 2052, Australia

⁴¹Patashnick Voorheesville Observatory, Voorheesville, NY 12186, USA

⁴²Instituto de Astrofísica, Pontificia Universidad Católica de Chile, Av. Vicuña Mackenna 4860, Macul, Santiago, Chile

⁴³Instituto de Astrofísica de Canarias, C. Vía Láctea S/N, E-38205 La Laguna, Tenerife, Spain

⁴⁴Universidad de La Laguna, Dept. de Astrofísica, E-38206 La Laguna, Tenerife, Spain

⁴⁵Department of Astrophysical Sciences, Princeton University, 4 Ivy Lane, Princeton, NJ 08544, USA

⁴⁶Department of Earth, Atmospheric and Planetary Sciences, Massachusetts Institute of Technology, Cambridge, MA 02139, USA

⁴⁷Department of Aeronautics and Astronautics, Massachusetts Institute of Technology, Cambridge, MA 02139, USA

⁴⁸NASA Ames Research Center, Moffett Field, CA 94035, USA

⁴⁹NASA Goddard Space Flight Center, Exoplanets and Stellar Astrophysics Laboratory (Code 667), Greenbelt, MD 20771, USA

(Received 2019 January 15; Revised 2020 October 27)

Submitted to AJ

ABSTRACT

We report the discovery of two short-period Saturn-mass planets, one transiting the G subgiant TOI-954 (TIC 44792534, $V = 10.343$, $T = 9.78$) observed in *TESS* Sectors 4 & 5, and one transiting the G dwarf EPIC 246193072 ($V = 12.70$, $K = 10.67$) observed in *K2* Campaigns 12 & 19. We confirm and characterize these two planets with a variety of ground-based archival and follow-up observations, including photometry, reconnaissance spectroscopy, precise radial velocity, and high-resolution imaging. Combining all available data, we find that TOI-954 b has a radius of $0.852^{+0.053}_{-0.062} R_J$ and a mass of $0.174^{+0.018}_{-0.017} M_J$ and is in a 3.68 d orbit, while EPIC 246193072 b has a radius of $0.774^{+0.026}_{-0.024} R_J$ and a mass of $0.260^{+0.020}_{-0.022} M_J$ and is in a 12.46 d orbit. As TOI-954 b is 30 times more irradiated than EPIC 246193072 b but is more or less of the same size, these two planets provide an opportunity to test whether irradiation leads to inflation of Saturn-mass planets and contribute to future comparative studies that explore Saturn-mass planets at contrasting points in their lifetimes.

Keywords: exoplanet systems, stars: individual (TIC 44792534, EPIC 246193072), techniques: photometric, techniques: spectroscopic

1. INTRODUCTION

Hot Saturns, with masses between 0.1 and $0.4 M_J$ and periods shorter than 20 d, are the lower-mass cousins of hot Jupiters (0.4 – $13 M_J$). Like hot Jupiters, hot Saturns’ relatively large sizes make it possible to detect their transits with small, ground-based telescopes (e.g. Brahm et al. 2018), and their short periods and relatively high masses make it possible to measure their masses with only a handful of ra-

dial velocity observations (e.g. Petigura et al. 2017). Space-based observatories like NASA’s *Transiting Exoplanet Survey Satellite* (*TESS*, Ricker et al. 2015) and the now-retired *Kepler* (Borucki et al. 2010), with their high photometric precision and nearly continuous observations, are especially well-suited to discover transiting hot Saturns en masse.

The occurrence rate of hot Saturns appears to be lower than other types of short-period exoplanets. Petigura et al. (2018) find that hot Saturns are intrinsically rarer than both hot Jupiters and hot Neptunes, even after accounting for selection effects. This occurrence rate “valley” may be an indication that hot Saturns are the smallest planets formed via run-away gas accretion. An in-depth study of their population can help us further understand the divergent formation pathways of small planets and gas giants.

The hot Saturns discovered thus far are in line with a broader trend that associates the presence of short-period

* Juan Carlos Torres Fellow

† NASA Sagan Fellow

‡ SNSF Ambizione Fellow

§ Packard Fellow

¶ Hubble Fellow

** NSF Fellow

†† Pappalardo Fellow

planets and that of large planets with higher host star metallicity (Mulders et al. 2016; Dong et al. 2018; Petigura et al. 2018). In fact, Petigura et al. (2018) find that hot Saturns (roughly corresponding to what they call “hot sub-Saturns”) have the highest mean stellar metallicity among all period and size bins. Virtually no hot Saturn has been found to orbit any metal-poor ($[\text{Fe}/\text{H}] < -0.05$) star, with the notable exceptions of HD 221416 b (Huber et al. 2019) and KELT-6 b (Collins et al. 2014). This evidence suggests some kind of mechanism connected to high stellar metallicity that leads to these short-period large planets.

Hot Saturns show a wide diversity in mean density, ranging from 0.09 to 5 g cm^{-3} . For planets of a similar size, hot Saturns tend to have large scatter in mass (Petigura et al. 2017). Because they have lower surface gravities than typical hot Jupiters, hot Saturns are some of the best targets for transmission spectroscopy observations (Wakeford et al. 2018). It is with this diversity and potential for future characterization in mind that we search for new transiting hot Saturns.

In this paper, we report the discovery of two hot Saturns, TOI-954 b and EPIC 246193072 b. As they orbit bright stars, we are able to confirm the two planets with precise radial velocity measurements. While the planets have similar sizes and masses and both orbit high-metallicity G stars, the two host stars are at different evolutionary stages: TOI-954 is evolved, while EPIC 246193072 is on the main sequence. Combining a more luminous host star and a smaller orbital distance, TOI-954 b is 30 times more irradiated than EPIC 246193072 b. This dramatic contrast allows us to probe a region of the parameter space where theories on planetary inflation are poorly tested.

Our paper is organized as follows. In § 2, we describe the observations leading to the detection and confirmation of those two planets. In § 3, we describe our data analysis procedures, and report our best estimates for the physical and orbital parameters for those systems. Finally, in § 4, we discuss those two new discoveries in the context of other known hot Saturns, focusing on reinflation and orbital eccentricity.

2. OBSERVATIONS

2.1. Photometry

In this subsection, we describe the photometric observations we use to perform our analysis. A summary of the observations can be found in Table 1. Light curves of TOI-954 are shown in Figure 1, and those of EPIC 246193072 are shown in Figure 2.

2.1.1. TESS Photometry

TESS observed TOI-954 in Sector 4 (UT 2018 October 18 – November 15) on Camera 2 CCD 2 and in Sector 5 (UT 2018 November 15 – December 11) on Camera 2 CCD 1 with a 30-minute cadence in the full frame images (FFIs). The MIT

Quick Look Pipeline (QLP) (Huang et al. 2019) detected the candidate with a signal to pink noise ratio of 52.4. The candidate showed consistent transit depths in all five apertures used by QLP and appeared to be on target in the difference image analysis. The TESS Science Office released the candidate as a TESS Object of Interest (TOI) after deeming it to have passed all the vetting criteria (Guerrero et al. submitted).

We used the SPOC-calibrated FFIs (Jenkins et al. 2016), obtained from the TESSCut service (Brasseur et al. 2019), to produce the detrended light curve used in this paper. We used a 45-pixel aperture (a 7×7 square without the four pixels at its corners) centered on the target. This aperture included an unresolved nearby star TIC 44792537 ($\Delta T = 3.29$, $48''.5$ separation, $\text{PA} = 153^\circ$) from the TESS Input Catalog (TIC 8; Stassun et al. 2019), which we would correct for by simultaneously fitting a dilution factor in the global model (§ 3.3). We rejected outliers due to spacecraft momentum dumps using the pointing quaternion time series. We also rejected cadences affected by stray light from Earth between JD 2458422.2 and 2458423.5 in Orbit 15 (Sector 4) (Fausnaugh et al. 2019a). No such stray light contamination affected Camera 2 in Sector 5 (Fausnaugh et al. 2019b). Orbit 15 was also affected by an instrument anomaly that prevented data collection from JD 2458418.54 to 2458421.21 (Fausnaugh et al. 2019a). We detrended the light curve by simultaneously modeling the spacecraft systematics, transits, and low-frequency variability following Vanderburg et al. (2016). As TESS observed the last transit of TOI-954 b close to the spacecraft’s perigee, the light curve was affected by excessive systematic noise, so we removed that transit from our subsequent analysis to obtain a more accurate transit depth.

2.1.2. K2 Photometry

EPIC 246193072 was observed in K2 Campaign 12 (UT 2016 December 15 – 2017 March 4) with the 29.4-minute long cadence as part of four GO programs¹. EPIC 246193072 was also observed during Campaign 19 (UT 2018 August 30 – September 26) as part of four long-cadence and one short-cadence (58.3 s) guest observer programs².

We initially identified the planet candidate in a Box Least Squares (BLS) search (Kovács et al. 2002; Vanderburg et al. 2016) of light curves produced by Vanderburg & Johnson (2014) in K2 data from Campaign 12. After identifying the planet candidate, we re-derived the Campaign 12 light curve by simultaneously modeling the spacecraft systemat-

¹ PIs: David Charbonneau, Andrew Howard, Dennis Stello, and Elisa Quintana.

² Short cadence PI: Andrew Vanderburg; long cadence PIs: Andrew Howard, Courtney Dressing, and Dennis Stello.

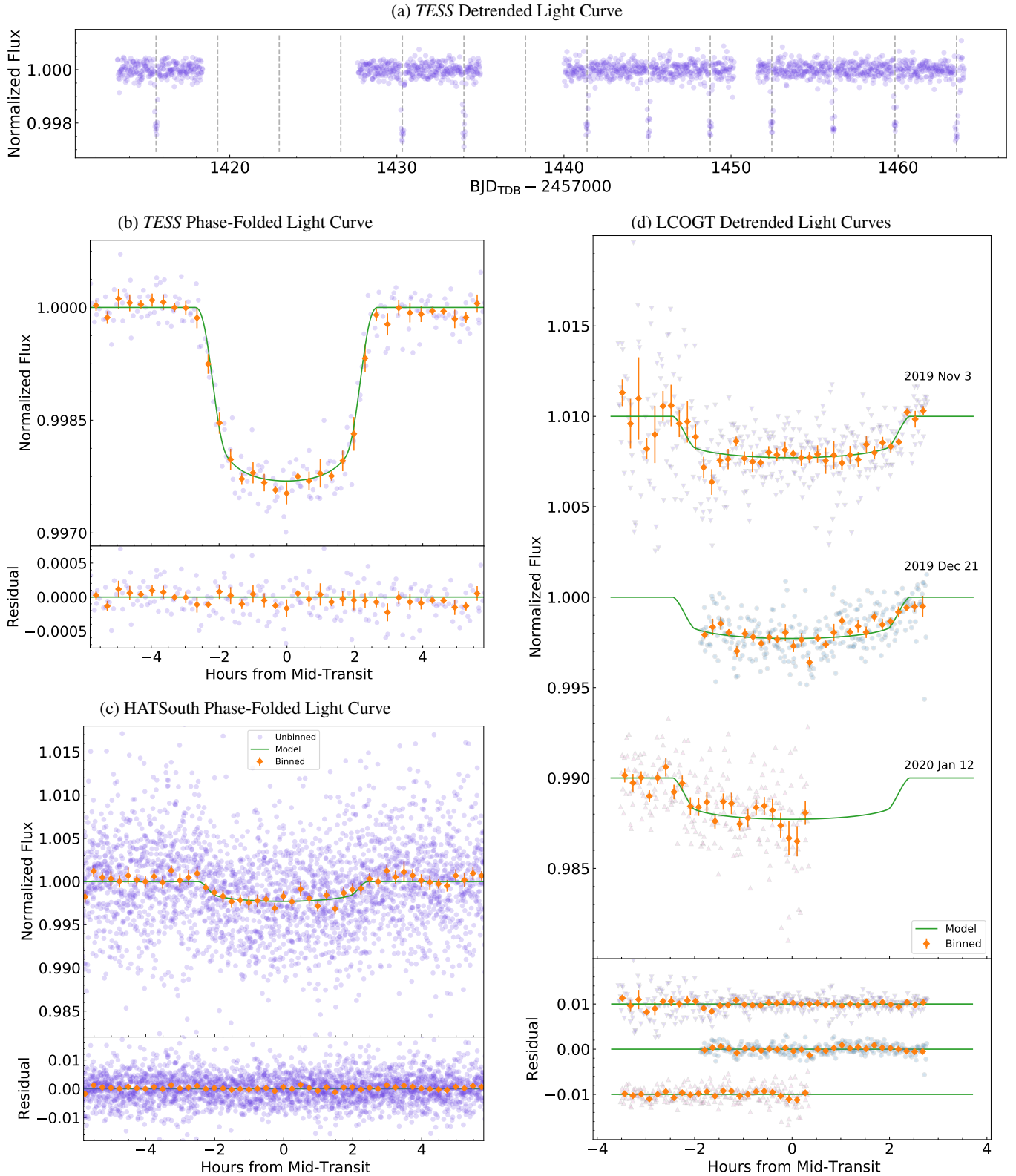


Figure 1. Light curves of TOI-954. The model plotted is the MCMC best-fit solution to the global model. The binned points indicate the mean of each bin, with error bars representing the standard error of the mean. (a) *TESS* detrended 30 min cadence light curve. (b) *TESS* detrended and phase-folded 30 min cadence light curve after correcting for dilution (§ 2.1.3), focusing on the transit. The bins are 20 min. (c) HATSouth TFA detrended and phase-folded light curve after correcting for dilution (§ 2.1.3), focusing on the transit. The bins are 15 min. The y-axes are restricted for the convenience of presentation, although the outliers are included in the per-bin calculations. (d) LCOGT detrended light curves. The bins are 10 min.

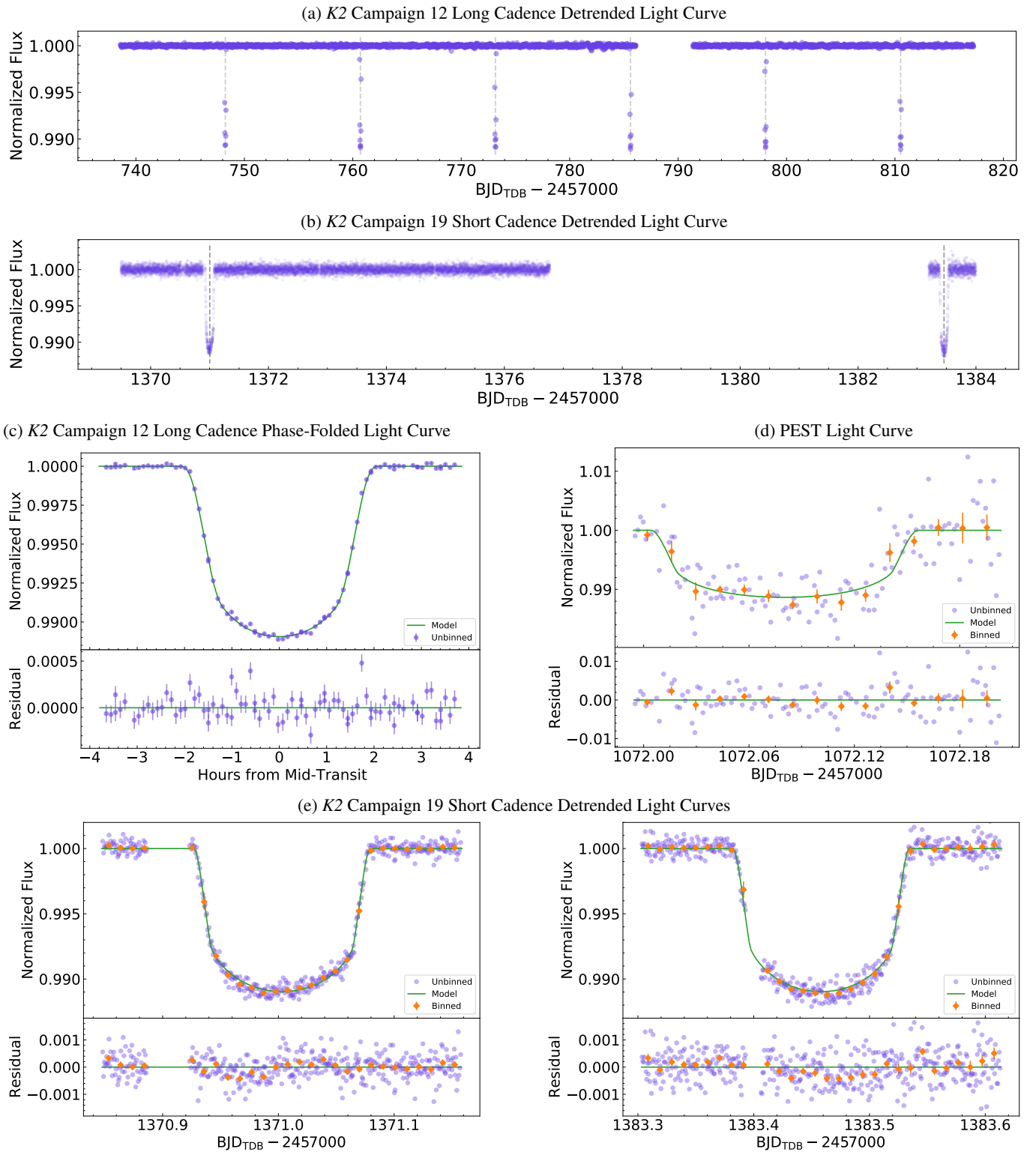


Figure 2. Light curves of EPIC 246193072. The model plotted is the MCMC best-fit solution to the global model. (a) K2 Campaign 12 long cadence detrended light curve. (b) K2 Campaign 19 short cadence detrended light curve. (c) K2 Campaign 12 long cadence detrended and phase-folded light curve. The noise is estimated from the out-of-transit portions of the light curve. (d) PEST observations. The binned points indicate the mean of each bin (20 min), with error bars representing the standard error of the mean. (e) K2 Campaign 19 short cadence detrended light curves. The two transits covered by this campaign are shown side-by-side. The binned points indicate the mean of each bin (15 min). The error bars are the standard error of the mean multiplied by a factor β that accounts for the excess red noise (§ 2.1.2). For the two transits, $\beta \approx 1.3$ and 1.6 , respectively.

ics, transits, and low-frequency variability following [Vanderburg et al. \(2016\)](#).

We took a more custom approach to reducing the Campaign 19 data. By the time *K2* began executing this campaign, it was critically low on fuel, so the spacecraft exhibited erratic pointing behavior and was only able to observe for about a month before completely exhausting its fuel reserves ([K2 Science Office 2020](#), accessed on 2020 Mar 4). Nevertheless, *K2* managed to achieve fairly typical pointing performance for about a week between UT 2018 September 8 and September 15, during which time EPIC 246193072 b transited once. We reduced the data collected during this time interval as usual, producing a first-pass light curve following [Vanderburg & Johnson \(2014\)](#) and refining the systematics correction with a simultaneous fit to the transit of EPIC 246193072 b, systematics, and low-frequency variability ([Vanderburg et al. 2016](#)).

After UT 2018 September 15, *K2*'s thruster corrections became less effective, and its pointing began to drift farther and less predictably than usual. We managed to recover a second usable transit of EPIC 246193072 b before the end of Campaign 19 by performing a simplified systematics correction to a 0.8 d window of data surrounding EPIC 246193072 b's transit. Here again, we simultaneously fit the transit of EPIC 246193072 b with a model for stellar variability and *K2* pointing systematics. This time, however, we did not attempt to separate the stellar variability from the spacecraft's pointing drift systematics, and modeled both with an aggressive basis spline (with knots spaced every 0.2 d instead of the typical 0.75 d used in a standard *K2* reduction), introducing a discontinuity when *K2* fired its thrusters (which only happened once during the 0.8 d window). We subtracted the best-fit spline from the original light curve to yield a systematics-free transit.

We estimated the excess red noise affecting the two transits in the Campaign 19 short cadence data following the method described by [Winn et al. \(2008\)](#). We calculated the β factor (the effective increase to flux uncertainty due to time-correlated noise) to be 1.3 for the first transit and 1.6 for the second, at a timescale comparable to the transit duration. Thus, we multiplied our white noise estimates for the two transits by their respective β factors to obtain the photometric uncertainties we used to calculate the global model posterior (§ 3.3).

2.1.3. Ground-based Follow-up Photometry

The HATSouth ([Bakos et al. 2013](#)) survey observed TOI-954 before *TESS* launched, for a total of 36 396 observations in the *r* band at an average of 6 min cadence from UT 2014 September 9 to 2015 March 6. The star was slightly saturated for the HATSouth observation, but with the help of the Trend Filtering Algorithm (TFA; [Kovács et al. 2005](#)), we were able

to pick up the signal in the light curve. While we were not able to use the HATSouth light curve to confirm whether the transit is on target, its long baseline helped us improve the precision of the planet's orbital period by an order of magnitude. We listed the measurement data in Table 2.

TOI-954 was also observed as part of the *TESS* Follow-up Program (TFOP). We attempted to observe an ingress on UT 2019 August 3 from the 0.7 m PlaneWave CDK700 telescope at Mauna Kea Observatories, Hawaii, stopping at twilight. The limited precision of the light curve prevented us from either confirming or ruling out the ingress, but we were able to rule out that the transit could have been caused by background eclipsing binaries within 40". The light curve time series can be found on the ExoFOP-TESS³ website.

A full transit of TOI-954 was observed in the Pan-STARSS z_s band on UT 2019 November 3, December 21, and 2020 January 12 using a 1.0 m telescope at the LCOGT South African Astronomical Observatory (SAAO) node in Sutherland, South Africa. The LCOGT observations were calibrated with the standard BANZAI pipeline and the light curves were extracted using ASTROIMAGEJ (AIJ; [Collins et al. 2017](#)). The observation used a 6" aperture, and recovered the expected transit signal. The detrended light curves can also be found on the ExoFOP-TESS website. The UT 2019 December 21 data were not included in the global model fitting (§ 3.3) because they did not contain enough out-of-transit observations to allow us to accurately measure the transit depth.

EPIC 246193072 was observed by the Perth Exoplanet Survey Telescope (PEST) on UT 2017 November 14, with 117 observations at 120 s cadence in the R_c band. PEST is a 12" Meade LX200 SCT Schmidt-Cassegrain telescope equipped with a SBIG ST-8XME camera located in a suburb of Perth, Australia. The PEST pipeline automatically reduced and calibrated the images, producing a light curve, which was normalized for transit model fitting ([Tan n.d.](#)). The transit arrived on time, and we were able to recover a full transit of the planet (Figure 2(c)), allowing us to improve the precision of the planet's orbital period. We reported the measurement data in Table 3.

EPIC 246193072 was also observed by the 24" telescope at the Peter van de Kamp Observatory of Swarthmore College, Pennsylvania on UT 2018 July 9. We made 78 measurements in the r' filter with an exposure time of 90 s. We observed an egress of EPIC 246193072 b on the expected target under good sky conditions. We decided to not include this partially observed transit in our global model fitting (§ 3.3).

2.2. Spectroscopy

³ <https://exofop.ipac.caltech.edu/tess/target.php?id=279741379>

Table 1. Summary of Photometric Observations

Instrument & Field	UT Date(s)	No. Images ^a	Cadence second	Filter	Additional Parameter
TOI-954					
TESS Sector 4 Camera 2 CCD 2	2018 Oct 18 – Nov 15	732	1800	TESS	$D = 0.0363^{+0.0046b}_{-0.0045}$
TESS Sector 5 Camera 2 CCD 1	2018 Nov 15 – Dec 11	1074	1800	TESS	
HATSouth	2014 Sep 9 – 2015 Mar 6	22351	370 ^c	<i>r</i>	$D = (0.9^{+1.5}_{-0.7}) \times 10^{-5b}$
LCOGT SAAO 1 m	2019 Nov 3	396	30	<i>z_s</i>	$C = 1.809^{+0.052d}_{-0.049}$
LCOGT SAAO 1 m	2019 Dec 21 ^e	299	30	<i>z_s</i>	
LCOGT SAAO 1 m	2020 Jan 12	250	30	<i>z_s</i>	
EPIC 246193072					
K2 Campaign 12	2016 Dec 15 – 2017 Mar 04	3314	1764	<i>Kepler</i>	—
K2 Campaign 19	2018 Aug 30 – Sep 26	11595	59	<i>Kepler</i>	—
PEST	2017 Nov 14	117	120	<i>R_c</i>	Jitter = 0.00232 ± 0.00037^f
PvdK 24 ^{''e}	2018 Jul 9	78	90	<i>r'</i>	—

^aExcluding frames flagged for instrumental or quality issues and outliers over 4σ (when out of transit).

^bDilution correction factor applied to the detrended light curve, defined as the ratio of contaminating flux to total flux.

^cMultiplicative factor applied to the quoted noise of the LCOGT light curves.

^dEstimated by taking the median time elapsed between consecutive exposures and rounding to the nearest ten seconds.

^eNot used for the global model fitting (§ 3.3).

^fJitter is added in quadrature to the reported noise during the global model fitting.

We now describe the spectroscopic observations we use to confirm the planets of TOI-954 and of EPIC 246193072. A summary of those observations can be found in Table 4.

2.2.1. Reconnaissance Spectroscopy

Three spectra of TOI-954 were taken with the echelle spectrograph on the Australia National University (ANU) 2.3 m telescope for TOI-954 from UT 2019 February 18 to 2019 February 22, covering the wavelength region of 3900 to 6700 Å with a spectral resolution $R \approx 23000$. These spectra can be found on the ExoFOP-TESS website. The observations suggested that there was no radial velocity variation on the order of 500 m s^{-1} . We therefore moved on to higher-precision instruments for mass measurements of TOI-954 b.

The Tillinghast Reflector Echelle Spectrograph (TRES; Szentgyorgyi 2004) on the 1.5 m telescope at Fred L. Whipple Observatory, Arizona was used to obtain spectra for both TOI-954 (UT 2019 March 1) and EPIC 246193072 (UT 2017 September 10 & 28). TRES is a fiber-fed echelle spectrograph with a spectral resolution of $R \approx 44000$ over the wavelength region of 3850 to 9100 Å. The observing strategy and

data reduction process were described by Buchhave et al. (2012). Each spectrum was obtained from a combination of three consecutive observations for optimal cosmic ray rejection, and the wavelength solution was provided by bracketing ThAr hollow cathode lamp exposures. The TRES spectra used in this paper can be found on the ExoFOP-TESS and ExoFOP-K2⁴ websites.

We did not find evidence of strong stellar activity for either TOI-954 or EPIC 246193072 in the TRES spectra. The Ca II HK emission lines were absent.

EPIC 246193072 was also observed with the Fibre-fed Echelle Spectrograph (FIES; Frandsen & Lindberg 1999; Telting et al. 2014) mounted at the 2.56 m Nordic Optical Telescope (NOT) of Roque de los Muchachos Observatory (La Palma, Spain). The observations⁵ were carried out on two nights (UT 2017 August 16 and 18) using the high-resolution fiber, which provides a resolving power of 67000

⁴ https://exofop.ipac.caltech.edu/k2/edit_target.php?id=246193072

⁵ Part of the observing program 55-019, PI: D. Gandolfi

Table 2. HATSouth Photometric Measurements of TOI-954

BJD _{TDB} – 2400000	Raw Mag.	EPD Mag.	TFA Mag.	Uncertainty	Flag
56983.74903	10.41281	10.35094	10.34490	0.00121	0
56983.75455	10.40697	10.34580	10.34342	0.00121	1
56983.75856	10.40240	10.33414	10.34393	0.00121	0
56983.76259	10.39569	10.32704	10.33661	0.00120	1
56983.76884	10.39573	10.34297	10.34667	0.00121	0
56983.77290	10.40901	10.33885	10.34718	0.00121	0
56983.77695	10.40787	10.34479	10.34520	0.00121	0
56983.78253	10.40622	10.33925	10.33945	0.00121	1
56983.78654	10.40170	10.33649	10.33636	0.00121	1
56983.79106	10.40960	10.34238	10.34526	0.00121	0
56983.79659	10.41026	10.34137	10.34823	0.00121	1
56983.80074	10.41835	10.35022	10.34657	0.00122	0
56983.80476	10.41969	10.34276	10.34678	0.00122	0
56983.81011	10.41058	10.32626	10.34037	0.00121	0
56983.81468	10.42444	10.36145	10.35338	0.00122	1
56983.81878	10.42908	10.36117	10.35667	0.00122	0
56983.82426	10.42465	10.35300	10.34349	0.00122	1
56983.82834	10.42461	10.34070	10.34959	0.00122	1
56983.83246	10.43064	10.34189	10.35611	0.00123	0
56983.83846	10.42909	10.34239	10.34314	0.00122	0
56983.84263	10.43798	10.34189	10.34984	0.00123	0
56983.84664	10.43480	10.33644	10.34282	0.00123	0
56983.85218	10.44484	10.34619	10.34190	0.00124	0
56983.85624	10.45349	10.34244	10.34576	0.00124	0
56983.86080	10.52435	10.33869	10.34762	0.00129	0
56983.86621	10.48563	10.34870	10.34910	0.00130	0
56983.87025	10.46183	10.33230	10.35159	0.00136	0
56984.51946	10.47864	10.36408	10.34731	0.00129	0
56984.52352	10.46848	10.35617	10.34055	0.00126	0
56984.52758	10.46211	10.34552	10.33378	0.00125	0
56984.53352	10.45185	10.32801	10.33251	0.00124	1
56984.53812	10.44663	10.32807	10.33958	0.00123	0
56984.54214	10.45214	10.34555	10.34681	0.00124	0
56984.54819	10.44286	10.34677	10.33815	0.00123	0
56984.55233	10.43931	10.33513	10.34743	0.00123	0
56984.55643	10.44049	10.34325	10.33722	0.00123	1
56984.56297	10.44801	10.35086	10.34400	0.00123	0
56984.56709	10.44393	10.34679	10.34967	0.00123	1
56984.57119	10.43688	10.34890	10.34800	0.00123	0
56984.57646	10.44848	10.36341	10.35508	0.00123	1
56984.58053	10.43158	10.35575	10.34443	0.00123	0

NOTE—Table 2 is published in its entirety in the machine-readable format. A portion is shown here for guidance regarding its form and content. Two detrended magnitudes are given: one using the External Parameter Decorrelation (EPD, Bakos et al. 2010) method, and one using the Trend Filtering Algorithm (TFA, Kovács et al. 2005). A nonzero flag value indicates that an observation is affected by anomalously high systematics and excluded from the global model.

in the wavelength range 3650 to 9125 Å. The observing strategy follows the one adopted for TRES observations.

2.2.2. Precise Radial Velocities

The high-precision radial velocity measurements used in this paper are presented in Table 5 and Figure 3 for TOI-954; those for EPIC 246193072 are presented in Table 6 and

Table 3. PEST Photometric Measurements of EPIC 246193072

HJD _{UTC} – 2400000	Magnitude	Uncertainty
58071.9943414	12.4795	0.0028
58071.9958805	12.4784	0.0027
58071.9974061	12.4760	0.0027
58071.9989486	12.4769	0.0026
58072.0004769	12.4801	0.0026
58072.0035502	12.4791	0.0026
58072.0065972	12.4786	0.0026
58072.0081422	12.4858	0.0026
58072.0105639	12.4739	0.0026
58072.0136167	12.4806	0.0025
58072.0151562	12.4796	0.0026
58072.0167014	12.4796	0.0026
58072.0182275	12.4880	0.0026
58072.0197626	12.4888	0.0025
58072.0213111	12.4856	0.0026
58072.0228323	12.4875	0.0026
58072.0243530	12.4852	0.0025
58072.0268029	12.4946	0.0025
58072.0283283	12.4975	0.0026
58072.0298796	12.4847	0.0025
58072.0314200	12.4853	0.0025
58072.0329524	12.4924	0.0026
58072.0344828	12.4899	0.0025
58072.0360143	12.4882	0.0025
58072.0375664	12.4909	0.0025
58072.0391149	12.4869	0.0026
58072.0406562	12.4908	0.0025
58072.0431032	12.4904	0.0025
58072.0446452	12.4909	0.0025
58072.0461702	12.4891	0.0025
58072.0477101	12.4850	0.0025
58072.0492365	12.4907	0.0025
58072.0507722	12.4895	0.0025
58072.0523084	12.4847	0.0025
58072.0538298	12.4874	0.0025
58072.0553637	12.4916	0.0025
58072.0568884	12.4872	0.0025
58072.0593443	12.4892	0.0025
58072.0608676	12.4928	0.0025
58072.0624086	12.4914	0.0025

NOTE—Table 3 is published in its entirety in the machine-readable format. A portion is shown here for guidance regarding its form and content. We present the observation times in HJD_{UTC} as originally reported; however, they have been converted to BJD_{TDB} before inclusion in the global model (§ 3.3), following the methods described by Eastman et al. (2010). The magnitudes reported in this table are not detrended.

Figure 4. We now proceed to describe these observations in detail.

One of our main sources of precise radial velocity data was the iodine-fed Planet Finder Spectrograph (PFS; Crane et al. 2006, 2008, 2010) on the 6.5 m Magellan II Telescope at Las Campanas Observatory in Chile. TOI-954 was observed for a total of 8 radial velocities with a 20 min exposure time in

Table 4. Summary of Spectroscopic Observations

Instrument	UT Date(s)	No. Spectra	Resolution ^a $\Delta\lambda/\lambda/1000$	S/N Range (5000 Å)	Wavelengths Å	Jitter ms^{-1}	γ ms^{-1}
TOI-954							
ANU 2.3 m ^b	2019 Feb 18 – 22	3	23	49.6–75.8	3900–6700	—	—
CHIRON ^c	2019 Feb 22 – 27	5	80	67.7–76.1	4100–8700	$6.6^{+9.7}_{-4.7}$	-8826.0 ± 7.3
CORALIE	2019 Aug 19 – Sep 30	19	60	10.0–31.7	3900–6800	$4.9^{+4.2}_{-3.3}$	$-7347.2^{+3.0}_{-2.9}$
HARPS	2019 Sep 27 – 30	4	115	33.6–80.4	3780–6910	$2.5^{+4.3}_{-1.8}$	-7321.4 ± 2.1
MINERVA-Australis	2019 Sep 8 – Nov 10	12	80	— ^d	5000–6300	$16.0^{+5.7}_{-4.0}$	$8.2^{+5.5}_{-4.8}$
PFS	2019 Jul 11 – Sep 15	8	130	45–75	3910–7340	$6.8^{+3.5}_{-2.2}$	$-14.3^{+2.9}_{-2.6}$
TRES ^b	2019 Mar 1	1	44	30.3	3850–9096	—	—
EPIC 246193072							
FEROS	2017 Oct 14 – 2018 Jul 15	27	48	45–55	3500–9200	$17.0^{+3.4}_{-2.8}$	$-16999.0^{+4.1}_{-4.2}$
FIES ^b	2017 Aug 16 & 18	2	67	—	3650–9125	—	—
HARPS	2017 Nov 6 – 2018 Sep 6	13	115	17–35	3780–6910	$5.0^{+3.8}_{-3.1}$	-16982.9 ± 2.8
PFS	2018 May 24 – Oct 26	10	130	30–90	3910–7340	$3.7^{+1.7}_{-1.2}$	0.8 ± 1.4
TRES ^{b,c}	2017 Sep 10 & 28	2	44	26.8–31.3	3850–9096	—	—

^a Approximate values of typical instrument performance.

^b Reconnaissance spectroscopy; no radial velocities derived for the global model fitting (§ 3.3).

^c Spectra used to constrain the stellar parameters T_{eff} and metallicity.

^d The SNR estimate is unavailable; the RMS scatter from the median RV model is reported instead in § 2.2.2.

NOTE—The jitter parameter is added in quadrature to the reported RV uncertainties in Table 5 and Table 6. The γ parameter is a constant offset added to RV measurements of a given RV instrument. The jitter and γ values are empirically determined by a global model fit for each star system (see § 3.3).

2019 July and September for *TESS* follow-up. The iodine data and iodine-free templates were taken through a $0''.3$ slit, resulting in $R \approx 130000$. The mean internal uncertainty was 1.2 ms^{-1} , and the signal-to-noise ratio ranged from 45 to 75 in the iodine region at the peak of the blaze. EPIC 246193072 was observed between 2018 May and October for a total of 10 radial velocities for *K2* follow-up. The same $0''.3$ slit was used with 3×3 binning, resulting in $R \approx 43000$. The exposure times ranged from 33 to 50 min, achieving a signal-to-noise ratio of ~ 30 to 90 in the iodine region at the peak of the blaze and a mean internal uncertainty of 1.9 ms^{-1} . All PFS data were reduced with a custom IDL pipeline that flat-fielded, removed cosmic rays, and subtracted scattered light. Further details about the iodine-cell RV extraction method can be found in Butler et al. (1996).

The High Accuracy Radial velocity Planet Searcher (HARPS; Mayor et al. 2003) also contributed a significant portion of the precise radial velocity data used in this pa-

per. HARPS is fiber-fed by the Cassegrain focus of the 3.6 m telescope at La Silla Observatory in Chile. We obtained four spectra of TOI-954 during consecutive nights UT 2019 September 27 – 30 in good seeing conditions ($\sim 1''0$). The exposure time was 20 minutes, leading to a signal-to-noise ratio of 33.6–80.4 at 5000 Å. HARPS also observed EPIC 246193072 for two pairs of consecutive nights in UT 2017 November, five nights in UT 2018 July, and a pair of consecutive nights each in UT 2018 August and September, for a total of 13 spectra. We adopted exposure times of 1500 s and 1800 s for EPIC 246193072, which resulted in spectra with a signal-to-noise ratio per resolution element of 17–35.

The rest of the spectrographs observed either one of the two planets. The FEROS spectrograph (Kaufer et al. 1999), mounted on the MPG/ESO 2.2 m Telescope at La Silla observatory in Chile, observed 27 spectra of EPIC 246193072 at $R \approx 48000$ between UT 2017 October 14 and 2018 July 15. Each spectrum achieved a signal-to-noise ratio of 50

Table 5. Precise Radial Velocity Measurements of TOI-954

BJD	Radial Velocity ms^{-1}	Uncertainty ms^{-1}	Instrument
2458536.59568	-8812.91816	8.13894	CHIRON
2458538.60658	-8839.10797	17.70062	CHIRON
2458539.60827	-8800.58690	14.49605	CHIRON
2458540.59466	-8818.69516	18.01763	CHIRON
2458541.57702	-8844.42831	13.41980	CHIRON
2458714.906319	-7347.17	8.83	CORALIE
2458716.832690	-7329.20	9.01	CORALIE
2458718.846938	-7369.61	8.71	CORALIE
2458727.837791	-7325.22	8.84	CORALIE
2458729.867972	-7373.46	9.72	CORALIE
2458730.875885	-7334.57	11.22	CORALIE
2458739.756150	-7360.71	11.34	CORALIE
2458740.811585	-7361.33	10.84	CORALIE
2458741.835606	-7339.48	10.79	CORALIE
2458744.829962	-7349.56	11.96	CORALIE
2458745.737422	-7321.07	35.27	CORALIE
2458746.749066	-7325.21	14.84	CORALIE
2458747.815505	-7383.09	12.90	CORALIE
2458751.740085	-7355.34	15.11	CORALIE
2458752.761760	-7361.95	9.22	CORALIE
2458753.728396	-7302.87	17.82	CORALIE
2458754.766691	-7365.72	10.48	CORALIE
2458755.885741	-7363.77	9.77	CORALIE
2458756.781573	-7332.19	12.27	CORALIE
2458753.799037	-7303.56	3.63	HARPS
2458754.756737	-7324.01	2.46	HARPS
2458755.813724	-7340.08	1.49	HARPS
2458756.749928	-7310.85	2.72	HARPS
2458735.11924305	32.749	5.2134	MINERVA-Australis
2458737.17597222	-3.6402	4.8895	MINERVA-Australis
2458741.08650462	20.146	9.9089	MINERVA-Australis
2458742.09328703	34.614	13.336	MINERVA-Australis
2458743.08164351	27.424	10.512	MINERVA-Australis
2458758.09859953	1.6529	9.5847	MINERVA-Australis
2458776.07408564	35.803	8.5726	MINERVA-Australis
2458777.15123842	7.3249	4.8943	MINERVA-Australis
2458795.08677083	-7.3261	5.2078	MINERVA-Australis
2458796.16503472	-25.319	4.4132	MINERVA-Australis
2458797.08497685	-12.976	4.3832	MINERVA-Australis
2458798.21734953	-38.352	4.4889	MINERVA-Australis
2458675.92609	8.36	1.44	PFS
2458679.92171	10.10	1.17	PFS
2458682.90503	-8.29	1.08	PFS
2458683.94257	6.87	1.37	PFS
2458684.94079	-32.33	0.90	PFS
2458737.88787	-18.21	1.34	PFS
2458738.83838	0.00	1.27	PFS
2458741.83181	-14.90	1.13	PFS

NOTE— The radial velocities given represent absolute relative motion to the solar system barycenter, except for those from MINERVA-Australis and PFS, where the mean relative motion has been subtracted. See Table 4 for the constant radial velocity offsets derived by the global model for each instrument.

Table 6. Precise Radial Velocity Measurements of EPIC 246193072

BJD	Radial Velocity ms^{-1}	Uncertainty ms^{-1}	Instrument
2458040.70773863	-16990.7	10.5	FEROS
2458063.59792602	-17046.9	9.3	FEROS
2458064.54347944	-17008.4	9.1	FEROS
2458064.61015499	-17001.6	9.5	FEROS
2458065.63009163	-16991.1	10.6	FEROS
2458065.57747400	-16978.0	9.0	FEROS
2458067.51507559	-16972.5	8.1	FEROS
2458073.51680660	-17044.5	7.7	FEROS
2458261.90205817	-17043.0	7.6	FEROS
2458262.90253453	-16999.1	7.5	FEROS
2458262.88111421	-16986.3	8.3	FEROS
2458262.92396402	-17020.9	7.6	FEROS
2458263.90571009	-16992.3	7.6	FEROS
2458263.92368049	-16980.6	7.5	FEROS
2458263.88775467	-16995.1	7.5	FEROS
2458264.85218595	-17021.5	8.9	FEROS
2458264.87014076	-17000.3	8.0	FEROS
2458264.88809828	-16996.0	8.2	FEROS
2458264.83421933	-16995.5	9.1	FEROS
2458265.91063007	-17005.3	8.2	FEROS
2458265.85674146	-17025.6	9.0	FEROS
2458265.89267519	-17006.7	9.3	FEROS
2458265.87470911	-17004.9	8.5	FEROS
2458311.86733030	-17005.6	7.7	FEROS
2458312.83754233	-17014.2	7.1	FEROS
2458313.81862457	-17002.4	7.5	FEROS
2458314.78898939	-17003.7	9.2	FEROS
2458063.53094302	-17009.9	5.2	HARPS
2458064.52324815	-16987.5	6.8	HARPS
2458066.52560427	-16985.0	8.6	HARPS
2458067.55479447	-16972.1	5.5	HARPS
2458314.80212100	-16964.4	8.5	HARPS
2458316.79691151	-16974.2	17.3	HARPS
2458321.73828811	-16995.9	19.8	HARPS
2458322.75617163	-16993.3	17.2	HARPS
2458323.74986105	-17002.3	12.2	HARPS
2458332.75758515	-16970.9	7.3	HARPS
2458333.80634123	-16988.3	7.3	HARPS
2458366.64961358	-16954.1	6.8	HARPS
2458367.64086452	-16960.8	7.3	HARPS
2458262.89585	-18.20	2.40	PFS
2458264.89722	-1.71	2.67	PFS
2458295.92099	-1.29	1.44	PFS
2458297.89449	-23.55	1.48	PFS
2458298.87651	-24.14	1.51	PFS
2458355.79845	26.91	1.51	PFS
2458406.56625	17.06	2.02	PFS
2458408.56428	-0.47	2.01	PFS
2458415.55544	17.61	1.71	PFS
2458417.55814	25.62	2.11	PFS

NOTE— The radial velocities given represent absolute relative motion to the solar system barycenter, except for those from PFS, where the mean relative motion has been subtracted. See Table 4 for the constant radial velocity offsets derived by the global model for each instrument.

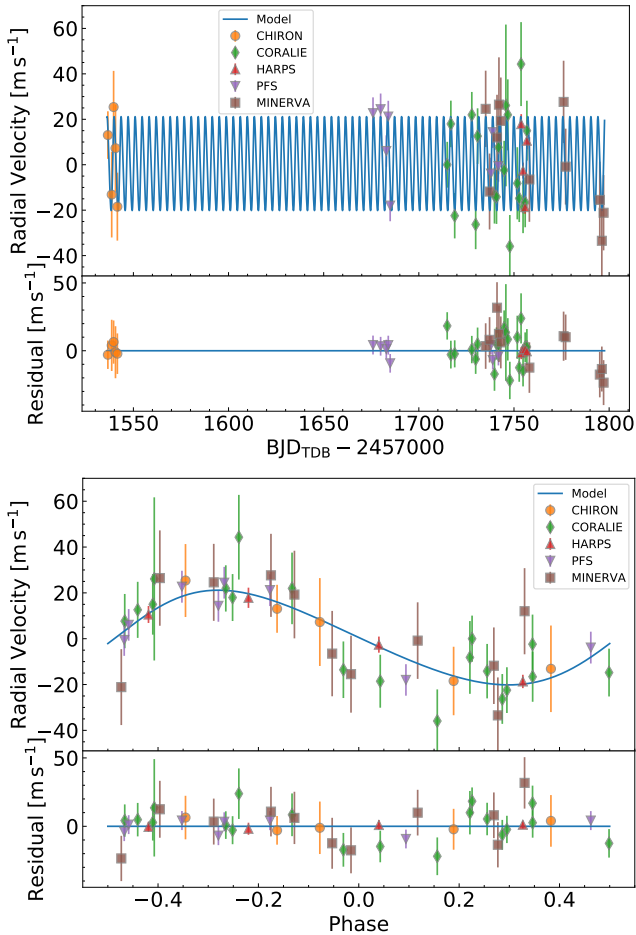


Figure 3. Precise radial velocity measurements of TOI-954. The model plotted is the MCMC median of the global model. A empirically derived per-instrument offset γ has been subtracted from the raw RV measurements. The error bars represent the reported uncertainty and the empirically derived per-instrument jitter, added in quadrature. These RV measurements are also listed in Table 5. *Top*—The RV measurements plotted against time. *Bottom*—Phase-folded RV measurements.

per spectral resolution element with exposure times of 1200 sec. The instrumental drift was determined via comparison with a simultaneous fiber illuminated with a ThAr+Ne lamp. The data were processed with the CERES suite of echelle pipelines (Brahm et al. 2017), which produce radial velocities and bisector spans in addition to reduced spectra.

The final two spectrographs observed TOI-954 only. We obtained a total of seven spectra using the CHIRON echelle spectrograph (Tokovinin et al. 2013) on the SMARTS 1.5 m Telescope located at the Cerro Tololo Inter-American Observatory (CTIO), Chile between UT 2019 February 22 and 27. CHIRON was fed via an image slicer and a fiber bundle, yielding a resolving power of $R \approx 80000$ over the wavelength range of 4100 to 8700 Å. Our observations were obtained at an exposure time of 900 s, achieving an average signal-to-

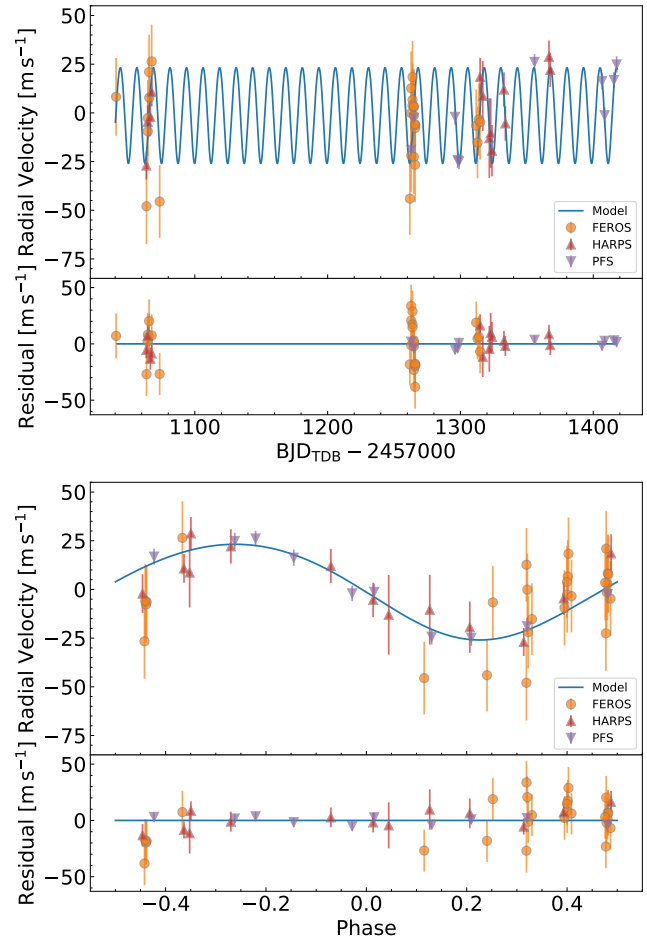


Figure 4. Precise radial velocity measurements of EPIC 246193072. The model plotted is the MCMC median of the global model. A empirically derived per-instrument offset γ has been subtracted from the raw RV measurements. The error bars represent the reported uncertainty and the empirically derived per-instrument jitter, added in quadrature. These RV measurements are also listed in Table 6. *Top*—The RV measurements plotted against time. *Bottom*—Phase-folded RV measurements.

noise ratio of 65 over the Mg b lines. Radial velocities were derived via a least-squares deconvolution between the observed spectra and synthetic non-rotating spectral templates generated via the ATLAS9 stellar models (Castelli & Kurucz 2004).

Last but not least, we observed TOI-954 with the fiber-fed spectrograph CORALIE ($R \approx 60000$, Queloz et al. 2001) on the Swiss 1.2 m Euler telescope located at La Silla Observatory (ESO, Chile). We acquired 19 RV measurements between UT 2019 August 19 and September 29, with the first CORALIE fiber on the star and the second one connected to a Fabry–Pérot etalon for simultaneous wavelength calibration, yielding a signal-to-noise ratio of 10.0–31.7 over the wavelength range of 3900 to 6800 Å. Radial velocities were computed for each epoch by cross-correlating with a G2 mask us-

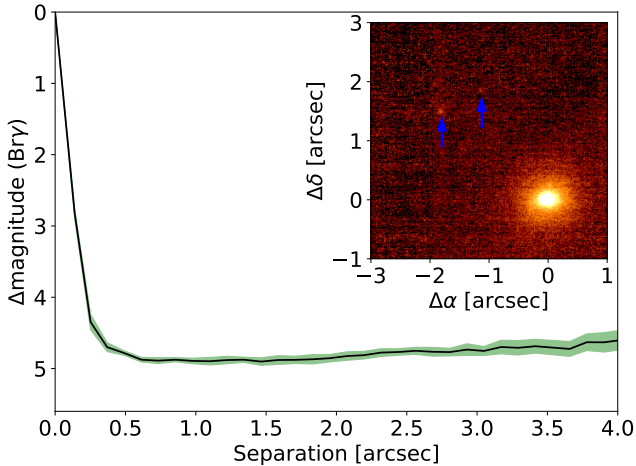


Figure 5. VLT/NaCo image of TOI-954, and sensitivity to background companions at close separations. The sensitivity is shown in the main plot, and the inset shows the central portion of the image itself, with the star offset so that the companions can be more clearly seen. Both visual companions are highlighted with blue arrows. The northern companion is a marginal detection of just 3σ , but the southern companion is well above our detection threshold.

ing the standard CORALIE Data Reduction Software (DRS, Pepe et al. 2002), which also produced various line-profile diagnostics such as cross-correlating bisector-span, FWHM, and contrast. The typical RV uncertainty achieved for the star was 11 m s^{-1} .

We observed TOI-954 with the MINERVA-Australis telescope array (Addison et al. 2019, 2020) at Mt. Kent Observatory in Queensland, Australia for 12 RV measurements between UT 2019 September 8 and November 10. MINERVA-Australis is a set of PlanetWave CDK700 telescopes connected by fibers to a single KiwiSpec R4-100 spectrograph (Barnes et al. 2012), yielding a resolution of $R \approx 80,000$ with wavelength coverage from 5000 to 6300 Å. We calculated the radial velocities using least-squares analysis, correcting for instrumental drift with simultaneous observations of a ThAr lamp. We measured an RMS scatter of 18 m s^{-1} from the median MCMC solution to the global model (§ 3.3). We discarded one RV measurement made on UT 2019 November 10 (BJD_{TDB} 2458798.2173) for the global model fitting (§ 3.3) because it was a $> 4\sigma$ outlier.

2.3. High Spatial Resolution Imaging

We collected AO images of TOI-954 with VLT/NAOS-CONICA (NaCo, Lenzen et al. 2003; Rousset et al. 2003) on UT 2019 September 14 to search for nearby companions. Nine exposures were collected in the Bry filter, each with an integration time of 30 s. The telescope was dithered by $2''$ between each individual image. We used a custom IDL code to process the data following standard practice: bad pixels were removed, data were flat fielded, a sky background was

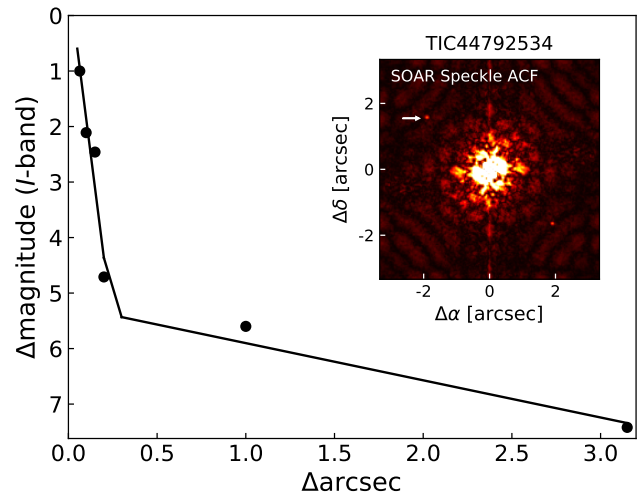


Figure 6. SOAR observation of TOI-954. The 5σ detection sensitivity is plotted with the speckle imaging auto-correlation function (ACF) inset. The companion is mirrored in the ACF, but its true position (PA = 50°) is marked with an arrow.

constructed from the dithered frames and subtracted, and the images were finally aligned and coadded. When visually inspecting the data, we found two visual companions: a firm detection of a companion at $2''.3$ and a marginal detection of a companion at $2''.1$, at approximately 3σ . Both companions are to the NE of the target, and are mutually separated by 781 mas.

We calculate our sensitivity to background stars by injecting model companions into the data and scaling their brightness until they are detected at 5σ . This process is repeated at a range of angles and radii, and the final sensitivity averaged azimuthally. The brighter companion is masked out during this sensitivity calculation. A plot of the sensitivity to companions is shown in Figure 5, which also includes a thumbnail image of the target with the two companions highlighted.

We also searched for nearby sources to TOI-954 with SOAR speckle imaging (Tokovinin 2018) on UT 2019 August 12, observing in a similar visible bandpass as *TESS*. Further details of the observations are available from Ziegler et al. (2020). Confirming the finding from NaCo, a faint companion ($\delta m_I = 6.2$) was detected at a separation of $2''.35$. The contamination from the star is negligible, implying a planetary radius correction factor of 1.002 due to dilution of the transit depth. The 5σ detection sensitivity and the speckle auto-correlation function from the SOAR observation are plotted in Figure 6.

We acquired speckle imaging data of EPIC 246193072 with the NN-Explore Exoplanet Stellar Speckle Imager (NESSI, Scott et al. 2018) installed on the 3.5 m telescope at WIYN Observatory on two nights, UT 2017 August 14 and September 5. The observations were in two passbands, 562 and 832 nm. Plots of the contrast curves with reconstructed

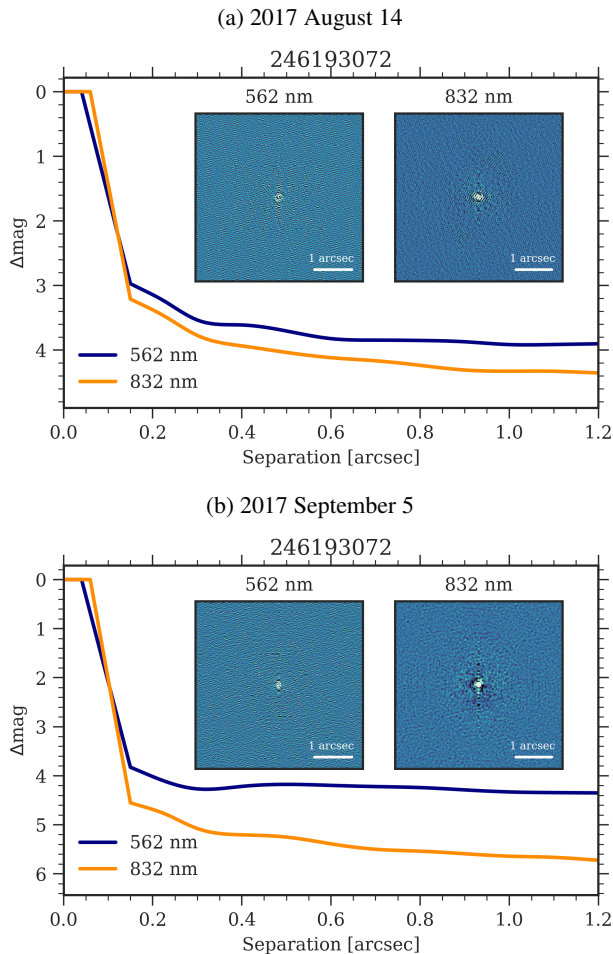


Figure 7. WIYN observations of EPIC 246193072 on UT 2017 August 14 (*Top*) and UT 2017 September 5 (*Bottom*). The 5σ contrast curves are plotted with the reconstructed images. No companions are detected.

images inset can be found in Figure 7. The conditions were slightly more favorable on September 5, which led to better contrast in both channels. No companions were detected.

3. ANALYSIS

3.1. Confirmation of TOI-954 b and EPIC 246193072 b

Our follow-up observations rule out common astrophysical false positives that may be mistaken for a transiting planet. The transit signals for both TOI-954 b and EPIC 246193072 b are confirmed to be on-target by ground-based observations. We have also detected strong radial velocity signals matching the transit-derived orbital periods for both planets. We can rule out that the TOI-954 b signal is contaminated by the stars at a separation of $\sim 2''$ because the PFS slit ($0''.3$) excludes those sources. Speckle imaging did not detect any stars that could contaminate the signal of EPIC 246193072 b. Therefore, we confirm the two planets with high confidence.

3.2. Stellar Parameters

3.2.1. Reconnaissance Spectra

We used the Stellar Parameter Classification tool (SPC; Buchhave et al. 2012) to extract stellar parameters such as T_{eff} , $\log g$, metallicity, and $v \sin i$ from the TRES spectra. We were able to determine that TOI-954 is slightly evolved off the main sequence and that EPIC 246193072 is a main sequence star with $T_{\text{eff}} = (5359 \pm 50)$ K, $\log g = 4.6 \pm 0.1$, $[\text{Fe}/\text{H}] = 0.16 \pm 0.08$, and $v \sin i = (1.9 \pm 0.5)$ km s^{-1} .

Because we only obtained a relatively low signal-to-noise spectrum for TOI-954 from TRES, we opted to use the stellar parameters derived from the average of seven CHIRON spectra. The CHIRON spectra were calibrated against a library of ~ 10000 observed spectra classified by the SPC pipeline, interpolated via a gradient-boosting regressor. We derived $T_{\text{eff}} = (5710 \pm 51)$ K, $\log g = 4.00 \pm 0.05$, $[\text{Fe}/\text{H}] = 0.21 \pm 0.05$, and $v \sin i = (5.6 \pm 0.5)$ km s^{-1} for TOI-954 from the CHIRON spectra.

As a sanity check, we also determined the stellar parameters of EPIC 246193072 from the co-added FIES spectra. We followed the method outlined in Gandolfi et al. (2017) and used a customized IDL software suite that fitted spectral features sensitive to different photospheric parameters with ATLAS 9 model atmospheres (Castelli & Kurucz 2004). The results corroborated the stellar parameters derived from the TRES spectra to within 1σ .

The T_{eff} and $[\text{Fe}/\text{H}]$ of both stars are used as Gaussian priors in our global model fitting (§ 3.3). The $\log g$ values, however, are not used to constrain the global model, and thus serve as an independent check on the stellar density as constrained by the transit light curve.

3.2.2. Spectral Energy Distribution

As an independent check on the derived stellar parameters, we performed an analysis of the broadband spectral energy distribution (SED) together with the *Gaia* parallax in order to determine an empirical measurement of the stellar radius, following the procedures described by Stassun & Torres (2016); Stassun et al. (2017, 2018). We obtained the $B_T V_T$ magnitudes from Tycho-2, the $B V g r i$ magnitudes from APASS, the $J H K_S$ magnitudes from 2MASS, the W1–W3 magnitudes from WISE, the G magnitude from *Gaia*, and the GALEX NUV flux. Together, the available photometry spanned the full stellar SED over the wavelength range 0.2– $10 \mu\text{m}$ (see Figure 8).

We performed separate fits for TOI-954 and EPIC 246193072 using Kurucz stellar atmosphere models, with the priors on effective temperature (T_{eff}), surface gravity ($\log g$), and metallicity ($[\text{Fe}/\text{H}]$) from the reconnaissance spectroscopic values. The remaining free parameter was the extinction (A_V), which we limited to the maximum line-of-sight extinction from the Schlegel et al.

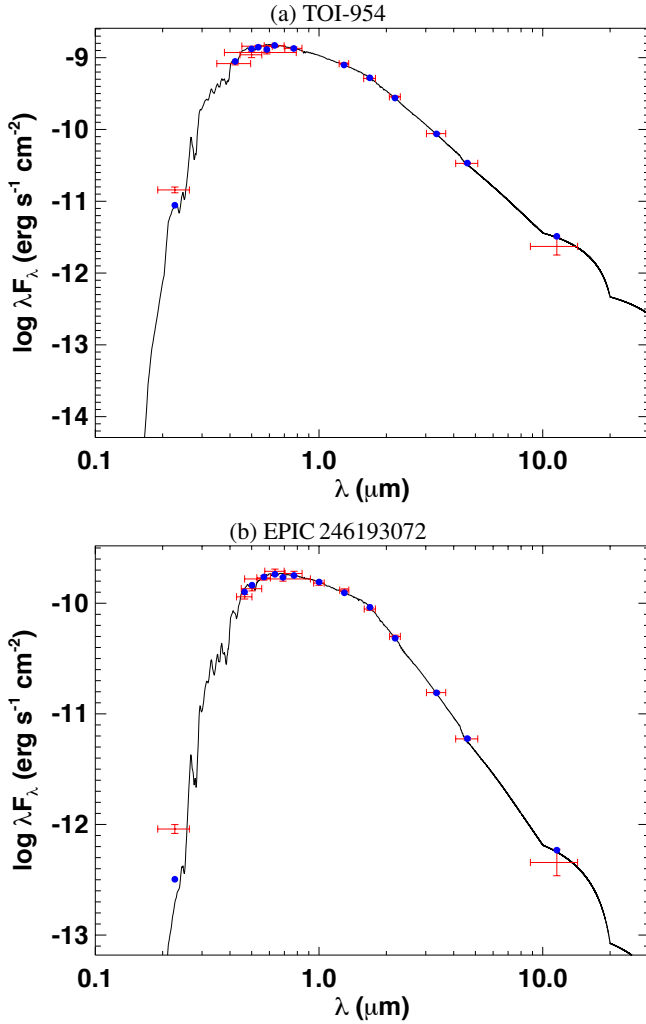


Figure 8. Spectral energy distribution (SED) for TOI-954 (*Top*) and EPIC 246193072 (*Bottom*). Red symbols represent the observed photometric measurements, where the horizontal bars represent the effective width of the passband. Blue symbols are the model fluxes from the best-fit Kurucz atmosphere model (black).

(1998) dust maps. The resulting fits were very good (Figure 8), with a reduced $\chi^2 = 2.3$ and a best fit extinction of $A_V = 0.06 \pm 0.06$ for TOI-954 and a reduced $\chi^2 = 1.58$ and a best fit $A_V = 0.09 \pm 0.03$ for EPIC 246193072. We adopted these A_V values as Gaussian priors for bolometric corrections in our global model (§ 3.3). The NUV flux of TOI-954 implies a modest level of chromospheric activity.

Integrating the unextinguished model SEDs gave the bolometric flux of $F_{\text{bol}} = (1.975 \pm 0.093) \times 10^{-9} \text{ erg s}^{-1} \text{ cm}^{-2}$ at Earth for TOI-954 and $F_{\text{bol}} = (2.880 \pm 0.033) \times 10^{-10} \text{ erg s}^{-1} \text{ cm}^{-2}$ at Earth for EPIC 246193072. Taking the F_{bol} and T_{eff} together with the *Gaia* parallax, adjusted by $+0.08 \text{ mas}$ to account for the systematic offset reported by Stassun & Torres (2018), gave stellar radii of

Table 7. Quadratic Limb Darkening Parameters

Filter	u_1	u_2
TOI-954		
<i>TESS</i>	$0.25^{+0.16}_{-0.14}$	$0.29^{+0.20}_{-0.19}$
<i>r</i>	$0.483^{+0.033}_{-0.034}$	$0.163^{+0.053}_{-0.051}$
z_s	0.32 ± 0.31	$0.199^{+0.057}_{-0.058}$
EPIC 246193072		
<i>Kepler</i>	0.535 ± 0.022	$-0.002^{+0.044}_{-0.045}$
R_c	$0.542^{+0.033}_{-0.033}$	$0.185^{+0.057}_{-0.059}$

NOTE—In the MCMC global modeling fit, we used the triangle sampling parametrization (q_1, q_2) of the quadratic limb darkening law by Kipping (2013). We used the least-squares values tabulated by Claret (2017) for *TESS* and Claret et al. (2013) for all other filters as Gaussian priors, taking the average deviation between the least-squares method and the flux-conservation method as the standard error. Here we report the posterior distribution (16th, 50th, and 84th percentiles) of the conventional (u_1, u_2) quadratic limb darkening parameters, converted from the MCMC samples of (q_1, q_2).

$(1.898 \pm 0.058) R_{\odot}$ for TOI-954 and $(0.804 \pm 0.017) R_{\odot}$ for EPIC 246193072.

3.3. Global Modeling

For each of the TOI-954 and the EPIC 246193072 planetary systems, we used the EMCEE Python package (Foreman-Mackey et al. 2013) to perform a global Markov Chain Monte Carlo (MCMC) model fit for planet properties, orbital parameters, and stellar properties. We ran the MCMC sampler over 500 000 iterations for each system, with 350 walkers for TOI-954 and 250 walkers for EPIC 246193072. We calculated the integrated autocorrelation time, or roughly the number of iterative steps it takes for a walker chain to generate an independent sample from the posterior distribution, following Goodman & Weare (2010) and empirically found it to be in the range of 7500 to 20 000 steps for the TOI-954 system model and 6000 to 11 000 steps for the EPIC 246193072 system model. Based on this autocorrelation timescale, we discarded the first 100 000 iterations as burn-in.

For each system, we modeled the detrended and normalized light curves (after rejecting out-of-transit outliers $> 4\sigma$) with the BATMAN package (Kreidberg 2015). In each model, we constrained the impact parameter so that the planet transits (i.e. $|b| < 1 + R_p/R_*$), and the radius of the planet is additionally constrained to be within 0.4 of the stellar radius. We also restricted the eccentricity to be less than 0.9 because the Kepler solver in BATMAN may fail at extremely high eccentricities. For each transit in the LCOGT, PEST, and *K2*

Campaign 19 data, we also simultaneously fitted and subtracted a weighted least-squares linear trend across the transit from the model residuals before calculating the χ^2 for the model posterior.

We added a variety of additional parameters to improve the light curves’ fit to the data; these additional parameters are reported in Table 1. We included a dilution factor for the *TESS* light curve with a Gaussian prior centered at 0.0460 and a width of 0.0046, which is the theoretical dilution from the unresolved star in our aperture calculated using *TESS* magnitudes in TIC 8. As the TFA detrending method tended to make transit depth shallower than the true transit in HATSouth light curves, we included an additional dilution factor in the model with a flat prior in $(0, 1)$. To account for possible underestimation of the noise of LCOGT and PEST measurements, we multiplied the quoted LCOGT noise by a factor ≥ 1 and added a nonnegative jitter term in quadrature to the quoted PEST noise as free parameters in their respective global model. We did not add any additional jitter to either the *TESS* or the *K2* light curves because the global model consistently preferred a value of zero during trial runs.

We note that the MCMC posterior solution for the TOI-954 system prefers a value much lower than the prior for the *TESS* light curve dilution factor. We believe that this apparent discrepancy arises because the dilution-corrected *TESS* light curve and the LCOGT light curves imply slightly different transit depths for the planet, which is captured by the global model in the larger uncertainties for the radius of TOI-954 b it reports.

We used the triangular sampling of the quadratic limb darkening law coefficients recommended by Kipping (2013), and constrained the coefficients using Gaussian priors. The priors were centered on values interpolated using the gradient boosting regressor in the SCIKIT-LEARN package from the least-squares fitted values tabulated by Claret (2017) for *TESS* and Claret et al. (2013) for all other filters. The posterior distribution of the quadratic limb darkening parameters are reported in Table 7.

We modeled the corresponding radial velocities with RADVEL (Fulton et al. 2018) in the joint fit. For each spectroscopic instrument, we introduced a constant offset term γ to the reported radial velocities and added a jitter term in quadrature with the reported errors, allowing the model to adjust each freely. The γ terms are unconstrained, while the jitter terms are constrained to be nonnegative. Those additional RV parameters are reported in Table 4. We did not find any statistically significant long-term trends in the RV measurements of either star.

To simultaneously constrain stellar properties, we fitted for initial stellar mass, initial stellar metallicity, and age in our global model. Those three parameters served as independent variables of the MIST isochrones (Dotter 2016; Choi et al.

2016), which we interpolated with the ISOCHRONES Python package (Morton 2015). We constrained the initial stellar mass to not exceed the valid range for the MIST isochrones $[0.1, 300]M_{\odot}$, and the stellar age to $[10^{-4}, 14]$ Gyr. The isochrone interpolation produced the current mass, metallicity ($[\text{Fe}/\text{H}]$), T_{eff} , and $\log g$ of the star, as well as the predicted *Gaia* absolute magnitudes. The transit light curves implicitly constrained the mass and $\log g$. To account for the theoretical uncertainty of the underlying stellar evolutionary model, we added a random Gaussian noise of 5% to the current stellar mass at each iterative step. We used the values derived from the reconnaissance spectra (CHIRON for TOI-954, TRES for EPIC 246193072; see § 2.2.1) as Gaussian priors for the metallicity and T_{eff} .

We used the three *Gaia* magnitudes G , G_{RP} , G_{BPto} to constrain the absolute magnitudes obtained from the isochrone interpolation. To apply bolometric corrections to the absolute magnitudes, we randomly drew values of A_V extinctions from a normal distribution based on the results of the independent SED analysis described in § 3.2.2. The isochrone-derived absolute magnitudes were then compared to those computed from the photometric and parallax measurements in *Gaia* DR2. We added an additional jitter, constrained to within $[0, 0.2)$, in quadrature to the three *Gaia* magnitudes as a free parameter to the model to account for additional systematic uncertainties. As with the independent SED analysis, we added a systematic offset of $(+0.082 \pm 0.033)$ mas reported by Stassun & Torres (2018) to the *Gaia* parallaxes.

The resulting posterior distributions show excellent fit with observations (Figures 1, 2, 3, & 4). The final median and 16th, 84th percentile values of the stellar and planetary system parameters are reported in Tables 8 & 9. Representative MCMC samples of the posterior distributions for the two models are reported separately in Tables 10 & 11.

We also ran an independent global analysis of the available photometric and radial velocity measurements of EPIC 246193072 using EXOFASTv2 (Eastman et al. 2013, 2019). The results of the EXOFASTv2 analysis were consistent ($< 1\sigma$) with the analysis described above in this section.

4. DISCUSSION

In order to understand how TOI-954 b and EPIC 246193072 b fit into the landscape of known planets, we compare them to transiting planets of similar size, mass, and period ($0.1 \leq M_p/M_J \leq 0.50$, $1 \leq M_p/M_J \leq 0.4$, $P < 20$ d) with mass measurement better than 50% and radius measurement better than 20% in Figure 9. This includes all “hot” giant planets around Saturn’s mass.

We use the parameters from the new Planetary Systems table on the NASA Exoplanet Archive website (Akeson et al. 2013, accessed on 2020 October 16). Unlike the traditional Confirmed Planets table, the Planetary Systems table

Table 8. Stellar Parameters

Parameter	Unit	TOI-954	EPIC 246193072	Source
Identifying Information				
α R.A. (J2015.5)	h:m:s	4 ^h 7 ^m 45 ^s .854	23 ^h 24 ^m 32 ^s .491	<i>Gaia</i> DR2
δ Decl. (J2015.5)	d:m:s	−25°12′31″.69	−5°9′50″.92	<i>Gaia</i> DR2
2MASS ID		J04074585-2512312	J23243247-0509507	TIC 8
TIC ID		44792534	301258470	TIC 8
Space observations		<i>TESS</i> Sectors 4 & 5	<i>K2</i> Campaigns 12 & 19	
Parallax ^a	mas	4.242±0.046	4.341±0.053	<i>Gaia</i> DR2
μ_α , R.A. proper motion . . .	mas yr ^{−1}	−5.787±0.042	14.169±0.063	<i>Gaia</i> DR2
μ_δ , decl. proper motion . . .	mas yr ^{−1}	−29.623±0.045	−12.389±0.052	<i>Gaia</i> DR2
Photometric Properties				
<i>TESS</i>	mag	9.779±0.006	11.904±0.006	TIC 8
<i>Kepler</i>	mag	—	12.463	EPIC
<i>B</i>	mag	11.153±0.063	13.542±0.070	TIC 8
<i>V</i>	mag	10.343±0.005	12.697±0.080	TIC 8
<i>J</i>	mag	9.180±0.024	11.174±0.023	TIC 8
<i>H</i>	mag	8.891±0.026	10.798±0.028	TIC 8
<i>K</i>	mag	8.779±0.023	10.668±0.023	TIC 8
<i>G</i>	mag	10.2321±0.0002	12.4462±0.0003	<i>Gaia</i> DR2
<i>G_{BP}</i>	mag	10.5978±0.0006	12.9023±0.0015	<i>Gaia</i> DR2
<i>G_{RP}</i>	mag	9.7328±0.0005	11.8537±0.0013	<i>Gaia</i> DR2
Jitter _{<i>G</i>} ^b	mag	0.026 ^{+0.052} _{−0.019}	0.039 ^{+0.080} _{−0.029}	Sampled
Stellar Properties				
T_{eff} , effective temperature	K	5710 ⁺⁵³ _{−49}	5282 ⁺⁴⁰ _{−39}	Derived
[Fe/H], metallicity	dex	0.215 ^{+0.050} _{−0.051}	0.098 ^{+0.065} _{−0.070}	Sampled
log <i>g</i> , surface gravity	dex	3.962 ^{+0.026} _{−0.024}	4.566 ^{+0.013} _{−0.021}	Derived
$v \sin i$, rotational speed	km s ^{−1}	5.6±0.5	1.9±0.5	Spectroscopy
M_* , mass	M_\odot	1.201 ^{+0.066} _{−0.064}	0.901 ^{+0.048} _{−0.049}	Sampled
R_* , radius	R_\odot	1.892 ^{+0.077} _{−0.076}	0.822 ^{+0.026} _{−0.024}	Derived
ρ_* , density	g cm ^{−3}	0.249 ^{+0.025} _{−0.021}	2.30 ^{+0.12} _{−0.16}	Derived
L_* , luminosity	L_\odot	3.43 ^{+0.24} _{−0.23}	0.473 ^{+0.033} _{−0.028}	Derived
Age	Gyr	6.14 ^{+0.30} _{−0.30}	1.8 ^{+2.2} _{−1.3}	Sampled

^aAdjusted by a systematic offset of (+0.082 ± 0.033) mas reported by [Stassun & Torres \(2018\)](#).

^bJitter_{*G*} is added in quadrature to the reported noise of the *G*, *G_{BP}*, and *G_{RP}* magnitudes during the global model fitting.

NOTE—The values from this work are the medians and the 16th and 84th percentiles of the MCMC-derived posterior distribution. All solar-scaled units in this paper are defined and calculated as the recommended nominal values adopted in IAU 2015 Resolution B3 ([Prša et al. 2016](#)).

References—Sampled: this work. Derived: Calculated from the sampled parameters with the MIST isochrone models ([Dotter 2016](#); [Choi et al. 2016](#)). Spectroscopy: Derived from reconnaissance spectra only; not part of the global model. EPIC: [Huber et al. \(2016\)](#). *Gaia* DR2: [Gaia Collaboration et al. \(2018\)](#). TIC 8: [Stassun et al. \(2019\)](#).

Table 9. Planetary and System Parameters

Parameter	Unit	TOI-954 b	EPIC 246193072 b
Sampled Parameters			
T_c , time of conjunction	BJD	2458411.90651 ^{+0.00084} _{-0.00078}	2457773.157267 ^{+0.000073} _{-0.000075}
P , period	day	3.6849729 ^{+0.000027} _{-0.000028}	12.4551225±0.0000031
K , RV semiamplitude	ms ⁻¹	20.7 ^{+2.0} _{-1.9}	24.6 ^{+1.6} _{-1.8}
$\sqrt{e} \sin \omega$		-0.35 ^{+0.49} _{-0.20}	0.081 ^{+0.089} _{-0.094}
$\sqrt{e} \cos \omega$		0.07 ^{+0.06} _{-0.13}	-0.23 ^{+0.13} _{-0.08}
$b \equiv a \cos i / R_\star$		0.56 ^{+0.04} _{-0.24}	0.364 ^{+0.039} _{-0.048}
R_p / R_\star		0.0462 ^{+0.0019} _{-0.0023}	0.09679 ^{+0.00056} _{-0.00057}
Derived Parameters			
T_{14} , total transit duration . .	hour	5.09 ^{+0.93} _{-0.37}	3.621 ^{+0.019} _{-0.017}
e , eccentricity		0.14 ^{+0.18} _{-0.11}	0.0697 ^{+0.041} _{-0.040}
e , eccentricity (95th percentile) .		0.37	0.140
ω , argument of periastron degree		276 ⁺⁹ ₋₁₇₄	161 ⁺²² ₋₃₀
a , semimajor axis	au	0.04963 ^{+0.00089} _{-0.00090}	0.1016 ^{+0.0018} _{-0.0019}
a / R_\star		5.63 ^{+0.18} _{-0.17}	26.62 ^{+0.46} _{-0.61}
i , inclination	degree	84.4 ^{+2.5} _{-0.6}	89.22 ^{+0.11} _{-0.09}
$M_p \sin i$, minimum mass	M_J	0.174 ^{+0.018} _{-0.017}	0.260 ^{+0.020} _{-0.022}
M_p , mass	M_J	0.174 ^{+0.018} _{-0.017}	0.260 ^{+0.020} _{-0.022}
R_p , radius	R_J	0.852 ^{+0.053} _{-0.062}	0.774 ^{+0.026} _{-0.024}
ρ_p , density	g cm ⁻³	0.35 ^{+0.10} _{-0.07}	0.694 ^{+0.070} _{-0.072}
Stellar irradiation	erg s ⁻¹ cm ⁻²	(1.896 ^{+0.090} _{-0.085}) × 10 ⁹	(6.22 ^{+0.30} _{-0.22}) × 10 ⁷
T_{eq} , equilibrium temperature ^a	K	1526 ⁺¹²³ ₋₁₆₄	650 ⁺⁵³ ₋₇₀

^a T_{eq} is calculated assuming no atmospheric redistribution and a uniformly random distribution of Bond albedo in the interval [0, 0.7).

NOTE—The values given are the medians and the 16th and 84th percentiles of the MCMC-derived marginalized posterior distribution. All Jupiter-scaled units in this paper are defined and calculated as the recommended nominal values adopted in IAU 2015 Resolution B3 (Prša et al. 2016). The Jupiter radius R_J is taken to be the equatorial radius.

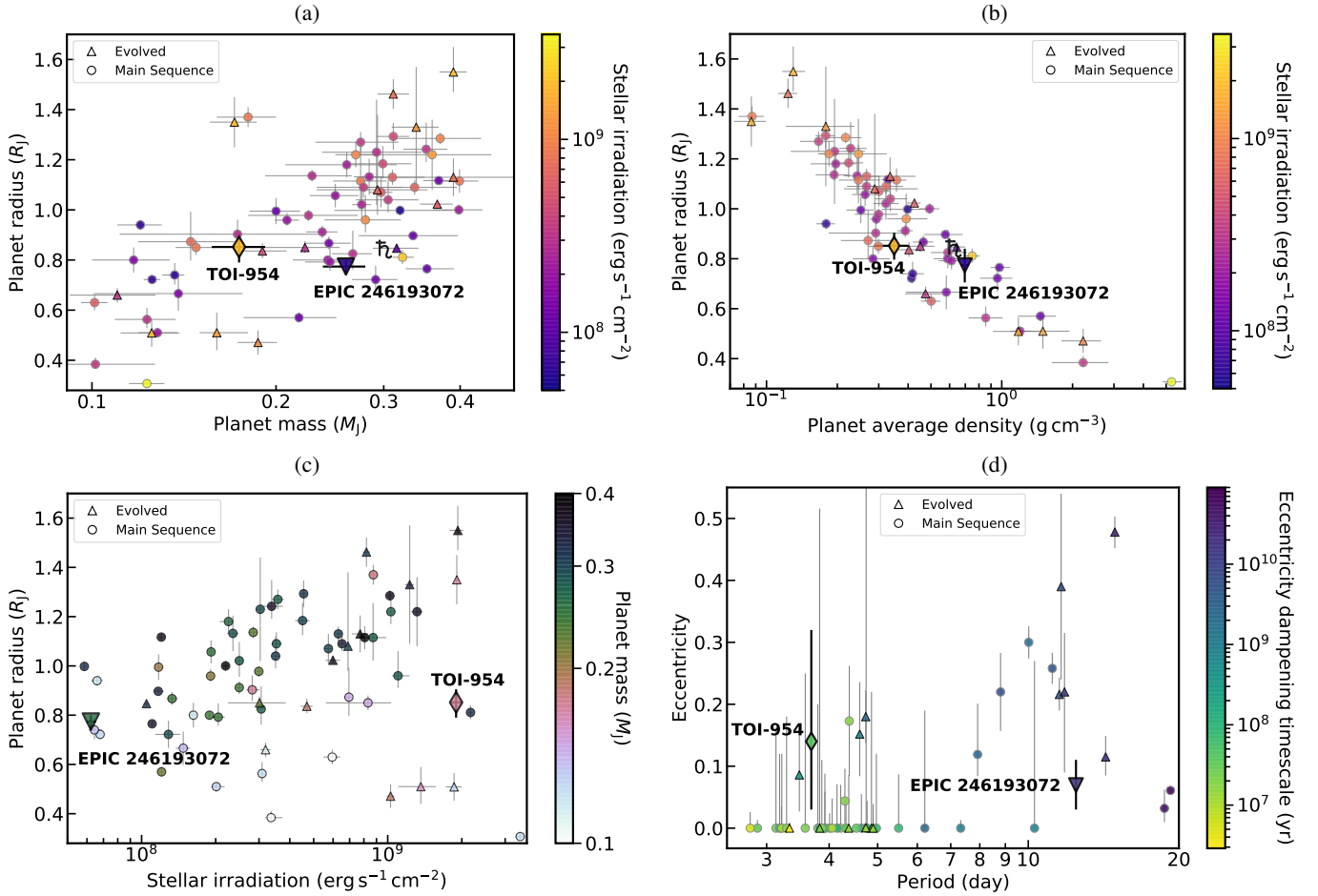


Figure 9. TOI-954 b and EPIC 246193072 b compared to planets of similar mass (measured to better than 50%) and period ($0.1 \leq M_p/M_J \leq 0.4$, $P < 20$ d). The planet parameters were retrieved from the NASA Exoplanet Archive on 2020 October 16 (Akeson et al. 2013), preferring those by Bonomo et al. (2017) where possible. Upright triangles represent planets around stars that are off the main sequence, while circles represent planets around stars on the main sequence. The evolutionary stage of the stars is determined by comparing the absolute *Gaia* G magnitude and the color using the *Gaia* G_{BP} and G_{RP} bands with the theoretical MIST terminal age main sequence isochrones. The planet Saturn is included in subfigures (a) and (b) for comparison. In subfigure (d), only planets with quoted uncertainties in eccentricity are plotted. Most of the plotted eccentricity upper limits are at the 2σ significance level, but a few are at 1 or even 3σ . We choose to present the upper limits in literature as-is, because it is impossible to convert the upper limits to a uniform significance level without access to their underlying posterior distributions. The eccentricity dampening timescale (τ_{ep}) is the characteristic time for tidal effects to circularize a planet’s orbit. It is calculated according to Equation (1) in Dobbs-Dixon et al. (2004) with the quality factor Q'_p assumed to be 10^5 .

presents all available planetary and stellar parameters from literature, so we are free to choose sets of parameters that produce more uniform results.

We use the following procedures to choose between different sets of parameters for a given planet:

1. We prefer the parameters from Bonomo et al. (2017) if available, because they provide eccentricity and mass measurements from HARPS-N for the largest number of the planets under consideration.
2. We prefer parameters with quoted uncertainties on eccentricity; that is, the fit allows eccentricity to vary rather than assuming circular orbit.

3. If there are more than one set of parameters with similar quoted uncertainties, we use the one with the “default parameter set” flag; that is, the one presented in the traditional Confirmed Planets Table).

Those procedures yield 65 planets that satisfy our selection criteria, 50 of which have quoted uncertainties on their eccentricity measurements.

4.1. Stellar Irradiation and Re-inflation

Both of our planets are around the lower ranges of mass and size for gas giants. TOI-954 b has about two thirds of the mass of EPIC 246193072 b, but its size is 10% larger. Figure 9(a) plots the measured masses and sizes and the derived stellar irradiation of the selected planets, highlighting the two

Saturn-sized planets from this work. Figures 9(b) and (c) cast the same information in different axes.

For our sample of hot Saturns, there is a weak positive correlation between a planet’s mass and size, but the scatter is large. A weak positive correlation has also been noted by Hatzes & Rauer (2015) and Chen & Kipping (2017) at the smaller end of gas giants, although they each used subtly different binning under which our planet population does not neatly fall. We consider further investigation of this weak correlation to be outside the scope of this work, and we make no further attempt to compare our results quantitatively.

Neither planet is appreciably inflated, compared to planets within the same mass bin, even though TOI-954 b receives 30 times the stellar irradiation of EPIC 246193072 b. We note that the first hot Saturn discovered by *TESS*, HD 221416 b, is also around an evolved star and has almost the same mass and radius within 1σ compared to TOI-954 b, but receives 5 times less stellar irradiation. Previous studies of giant planets have empirically derived a limit on stellar irradiation of $\langle S \rangle \approx 2 \times 10^8 \text{ erg s}^{-1} \text{ cm}^{-2}$, below which planet inflation is not usually observed (Demory & Seager 2011; Miller & Fortney 2011). EPIC 246193072 b, an uninflated Saturn orbiting a main-sequence host star with irradiation $\sim 6 \times 10^7 \text{ erg s}^{-1} \text{ cm}^{-2}$, fits this expectation.

However, that TOI-954 b remains uninflated around a moderately evolved star seems to contradict proposed mechanisms that explain the inflated radii of gas giants in terms of the current value of the stellar irradiation (Fortney et al. 2007; Burrows et al. 2007). Based on data available at the time, Hartman et al. (2016) found that the hot Jupiters with radii exceeding $1.5 R_J$ tend to be found around evolved stars rather than main sequence stars, possibly because the increased luminosity of evolved stars causes the hot Jupiter to inflate. At an age of 6 Gyr, which is more than 80% of the way through its total life span, TOI-954 gives us a rare example of an evolved star with a dense hot Saturn. One possible explanation for this apparent paradox is that the re-inflation mechanism is less effective for lower-mass giant planets, for which the core-to-envelope mass ratio is higher (Enoch et al. 2012; Miller & Fortney 2011). As uninflated hot Jupiters around evolved stars are precisely the kind of planets that ground-based surveys would miss, space-based exoplanet survey missions like *TESS* will be able to tell us how common such planets are.

4.2. Eccentricity and Tidal Circularization

Since TOI-954 b and EPIC 246193072 b differ in semimajor axes by a factor of two and are around stars at different life stages, we would like to investigate whether their nearly circular orbits are consistent with tidal dissipation. The posterior distributions for the eccentricities of both planets are consistent with that of a circular orbit once we account for

the bias towards higher eccentricities described by Lucy & Sweeney (1971). Nevertheless, the posterior distributions suggest that we cannot rule out a small but nonzero eccentricity at the 2σ level for either of the two planets on a purely observational basis.

The timescale for eccentricity dampening is given by Goldreich & Soter (1966) as

$$\tau_{\text{ep}} = \frac{4}{63} \frac{Q'_p}{n} \frac{M_p}{M_*} \left(\frac{a}{R_p} \right)^5, \quad (1)$$

where $n = \sqrt{GM_*/a^3}$ is the mean motion of the planet, and Q'_p is the modified tidal quality factor. Calculating or even estimating Q'_p is a notoriously hard problem. Here, we adopt a value of $Q'_p = 10^5$, assuming that it is not too different from the present best estimate for Saturn using Cassini observations of its moons (Lainey et al. 2017). Under this order-of-magnitude estimation, we calculate that the τ_{ep} for TOI-954 b is 0.04 Gyr and that for EPIC 246193072 b is 15 Gyr. This is consistent with TOI-954 b having circularized before reaching its current age, but the case for EPIC 246193072 b warrants closer inspection.

There are two possible explanations that can reconcile the apparently circular orbit of EPIC 246193072 b with its eccentricity dampening timescale, which is on the order of the current age of the universe. The first explanation is that the interior structure of EPIC 246193072 b is dramatically different from Saturn’s, such that its Q'_p is an order of magnitude smaller, which brings the τ_{ep} in line with the estimated age of the star. This is not implausible, given the huge uncertainties in estimating Q'_p from a theoretical basis (Goldreich & Soter 1966). The other explanation is that some mechanism other than tidal dissipation is responsible for circularizing the orbit of EPIC 246193072 b. This scenario rules out high-eccentricity migration as the formation pathway for EPIC 246193072 b, and instead points to disk migration or *in situ* formation as possible mechanisms. Either way, only future investigations into the interior structures and formation pathways of short-period giant planets could provide us with a definitive answer.

ACKNOWLEDGMENTS

This paper includes data collected by the *TESS* mission, which are publicly available from the Mikulski Archive for Space Telescopes (MAST). Funding for the *TESS* mission is provided by NASA’s Science Mission directorate. Resources supporting this work were provided by the NASA High-End Computing (HEC) Program through the NASA Advanced Supercomputing (NAS) Division at Ames Research Center for the production of the SPOC data products.

This paper includes data collected by the *K2* mission. Funding for the *K2* mission is provided by the NASA Science Mission directorate.

This research has made use of the Exoplanet Follow-up Observation Program website, which is operated by the California Institute of Technology, under contract with the National Aeronautics and Space Administration under the Exoplanet Exploration Program.

This work makes use of observations from the LCOGT network.

The HATSouth network is operated by a collaboration consisting of Princeton University (PU), the Max-Planck-Institut für Astronomie (MPIA), the Australian National University (ANU), and the Pontificia Universidad Católica de Chile (PUC). The station at Las Campanas Observatory (LCO) of the Carnegie Institute is operated by PU in conjunction with PUC, the station at the High Energy Spectroscopic Survey (H.E.S.S.) site is operated in conjunction with MPIA, and the station at Siding Spring Observatory (SSO) is operated jointly with ANU. Development of the HATSouth project was funded by NSF MRI grant NSF/AST-0723074, and operations have been supported by NASA grants NNX09AB29G, NNX12AH91H, and NNX17AB61G.

This paper includes observations made with the Nordic Optical Telescope (Prog. ID: 55-019), operated by the Nordic Optical Telescope Scientific Association at the Observatorio del Roque de los Muchachos, La Palma, Spain, of the Instituto de Astrofísica de Canarias.

This paper includes data gathered with the 6.5 m Magellan Telescopes located at Las Campanas Observatory, Chile.

This paper includes observations made with MINERVA-Australis. MINERVA-Australis is supported by Australian Research Council LIEF Grant LE160100001, Discovery Grant DP180100972, Mount Cuba Astronomical Foundation, and institutional partners University of Southern Queensland, UNSW Australia, MIT, Nanjing University, George Mason University, University of Louisville, University of California Riverside, University of Florida, and The University of Texas at Austin. We respectfully acknowledge the traditional custodians of all lands throughout Australia, and recognise their continued cultural and spiritual connection to the land, waterways, cosmos, and community. We pay our deepest respects to all Elders, ancestors and descendants

of the Giabal, Jarowair, and Kambuwal nations, upon whose lands the MINERVA-Australis facility at Mt Kent is situated.

This research is based on observations collected with the CORALIE echelle spectrograph mounted on the 1.2 m Swiss telescope and with the HARPS spectrograph on the ESO 3.6 m telescope at La Silla Observatory of the European Organisation for Astronomical Research in the Southern Hemisphere under ESO programme 0103.C-0874(A).

NESSI was funded by the NASA Exoplanet Exploration Program and the NASA Ames Research Center. NESSI was built at the Ames Research Center by Steve B. Howell, Nic Scott, Elliott P. Horch, and Emmett Quigley. The authors are honored to be permitted to conduct observations on Iolkam Du’ag (Kitt Peak), a mountain within the Tohono O’odham Nation with particular significance to the Tohono O’odham people.

We thank the Swiss National Science Foundation (SNSF) and the Geneva University for their continuous support to our planet search programs. This work has been in particular carried out in the frame of the National Centre for Competence in Research ‘PlanetS’ supported by SNSF. This publication makes use of The Data & Analysis Center for Exoplanets (DACE), which is a facility based at the University of Geneva dedicated to extrasolar planet data visualisation, exchange and analysis. DACE is a platform of the Swiss National Centre of Competence in Research (NCCR) PlanetS, federating the Swiss expertise in Exoplanet research. The DACE platform is available at <https://dace.unige.ch>.

This work is done under the framework of the KESPRINT collaboration (<http://kesprint.science>). KESPRINT is an international consortium devoted to the characterisation and research of exoplanets discovered with space-based missions.

A.J. and R.B. acknowledge support from FONDECYT Post-doctoral Fellowship Projects 1171208 and 3180246, respectively, and from ANID – Millennium Science Initiative – ICN12_009.

D.D. and J.K.T. acknowledge support provided by NASA through Hubble Fellowship grants HST-HF2-51372.001-A and HST-HF2-51399.001, respectively, awarded by the Space Telescope Science Institute, which is operated by the Association of Universities for Research in Astronomy, Inc., for NASA, under contract NAS5-26555.

I.J.M.C. acknowledges support from the NSF through grant AST-1824644,

J.H. is supported by SNSF through the Ambizione grant #PZ00P2_180098.

K.P. acknowledges support from NASA grant 80NSSC18K1009.

M.R.D. acknowledges the support of CONICYT/PFCHA-Doctorado Nacional-2014 21140646 Chile and Proyecto Basal AFB-170002.

M.T. is supported by MEXT/JSPS KAKENHI grant Nos. 18H05442, 15H02063, and 22000005.

This material is based upon work supported by the National Science Foundation Graduate Research Fellowship Program under Grant No. (DGE-1746045). Any opinions, findings, and conclusions or recommendations expressed in this material are those of the authors and do not necessarily reflect the views of the National Science Foundation.

Part of this research was carried out at the Jet Propulsion Laboratory, California Institute of Technology, under a contract with the National Aeronautics and Space Administration (NASA).

This work is partly supported by JSPS KAKENHI Grant Numbers JP18H01265 and JP18H05439, and JST PRESTO Grant Number JPMJPR1775.

L.S. would like to thank William S. Moses and MIT CSAIL for providing computing resources.

Software: AstroImageJ (Collins et al. 2017), Astropy (Astropy Collaboration et al. 2013, 2018), Batman (Kreid-

berg 2015), Emcee (Foreman-Mackey et al. 2013; Foreman-Mackey et al. 2019), EXOFASTv2 (Eastman et al. 2013, 2019), H5py, Isochrones (Morton 2015), Matplotlib (Hunter 2007), Numpy (Harris et al. 2020), MIT Quick Look Pipeline (Huang et al. 2019), TESS SPOC Pipeline (Jenkins et al. 2016; Twicken et al. 2018; Li et al. 2018), Pandas (Pandas Development Team 2020), Radvel (Fulton et al. 2018; Fulton et al. 2019), Scikit-learn (Pedregosa et al. 2011), Scipy (Virtanen et al. 2020), Tapir (Jensen 2013), TRES SPC (Buchhave et al. 2012), Vartools (Hartman & Bakos 2016).

Facilities: ATT (echelle spectrograph), CTIO:1.5m (CHIRON), ESO:3.6m (HARPS), Euler1.2m (CORALIE), FLWO:1.5m (TRES), *Gaia*, HATSouth, *Kepler* (K2), LCOGT (SAAO), Magellan:Clay (Planet Finder Spectrograph), Max Planck:2.2m (FEROS), MINERVA-Australis, MKO CDK700, NOT:2.56m (FIES), Perth Exoplanet Survey Telescope (PEST), Peter van der Kamp:0.6m, SOAR (HRCam), TESS, VLT:Antu (NaCo), WIYN (NESSI).

REFERENCES

- Addison, B., Wright, D. J., Wittenmyer, R. A., et al. 2019, *PASP*, 131, 115003, doi: [10.1088/1538-3873/ab03aa](https://doi.org/10.1088/1538-3873/ab03aa)
- Addison, B. C., Wright, D. J., Nicholson, B. A., et al. 2020, arXiv e-prints, arXiv:2001.07345. <https://arxiv.org/abs/2001.07345>
- Akeson, R. L., Chen, X., Ciardi, D., et al. 2013, *PASP*, 125, 989, doi: [10.1086/672273](https://doi.org/10.1086/672273)
- Astropy Collaboration, Robitaille, T. P., Tollerud, E. J., et al. 2013, *A&A*, 558, A33, doi: [10.1051/0004-6361/201322068](https://doi.org/10.1051/0004-6361/201322068)
- Astropy Collaboration, Price-Whelan, A. M., Sipőcz, B. M., et al. 2018, *AJ*, 156, 123, doi: [10.3847/1538-3881/aabc4f](https://doi.org/10.3847/1538-3881/aabc4f)
- Bakos, G. Á., Torres, G., Pál, A., et al. 2010, *ApJ*, 710, 1724, doi: [10.1088/0004-637X/710/2/1724](https://doi.org/10.1088/0004-637X/710/2/1724)
- Bakos, G. Á., Csubry, Z., Penev, K., et al. 2013, *PASP*, 125, 154, doi: [10.1086/669529](https://doi.org/10.1086/669529)
- Barnes, S. I., Gibson, S., Nield, K., & Cochrane, D. 2012, in *Proc. SPIE*, Vol. 8446, 844688, doi: [10.1117/12.926527](https://doi.org/10.1117/12.926527)
- Bonomo, A. S., Desidera, S., Benatti, S., et al. 2017, *A&A*, 602, A107, doi: [10.1051/0004-6361/201629882](https://doi.org/10.1051/0004-6361/201629882)
- Borucki, W. J., Koch, D., Basri, G., et al. 2010, *Science*, 327, 977, doi: [10.1126/science.1185402](https://doi.org/10.1126/science.1185402)
- Brahm, R., Jordán, A., & Espinoza, N. 2017, *PASP*, 129, 034002, doi: [10.1088/1538-3873/aa5455](https://doi.org/10.1088/1538-3873/aa5455)
- Brahm, R., Hartman, J. D., Jordán, A., et al. 2018, *AJ*, 155, 112, doi: [10.3847/1538-3881/aaa898](https://doi.org/10.3847/1538-3881/aaa898)
- Brasseur, C. E., Phillip, C., Fleming, S. W., Mullally, S. E., & White, R. L. 2019, *Astrocut: Tools for creating cutouts of TESS images*. <http://ascl.net/1905.007>
- Buchhave, L. A., Latham, D. W., Johansen, A., et al. 2012, *Nature*, 486, 375, doi: [10.1038/nature11121](https://doi.org/10.1038/nature11121)
- Burrows, A., Hubeny, I., Budaj, J., & Hubbard, W. B. 2007, *ApJ*, 661, 502, doi: [10.1086/514326](https://doi.org/10.1086/514326)
- Butler, R. P., Marcy, G. W., Williams, E., et al. 1996, *PASP*, 108, 500, doi: [10.1086/133755](https://doi.org/10.1086/133755)
- Castelli, F., & Kurucz, R. L. 2004, *ArXiv Astrophysics e-prints*. <https://arxiv.org/abs/astro-ph/0405087>
- Chen, J., & Kipping, D. 2017, *ApJ*, 834, 17, doi: [10.3847/1538-4357/834/1/17](https://doi.org/10.3847/1538-4357/834/1/17)
- Choi, J., Dotter, A., Conroy, C., et al. 2016, *ApJ*, 823, 102, doi: [10.3847/0004-637X/823/2/102](https://doi.org/10.3847/0004-637X/823/2/102)
- Claret, A. 2017, *A&A*, 600, A30, doi: [10.1051/0004-6361/201629705](https://doi.org/10.1051/0004-6361/201629705)
- Claret, A., Hauschildt, P. H., & Witte, S. 2013, *A&A*, 552, A16, doi: [10.1051/0004-6361/201220942](https://doi.org/10.1051/0004-6361/201220942)
- Collins, K. A., Kielkopf, J. F., Stassun, K. G., & Hessman, F. V. 2017, *AJ*, 153, 77, doi: [10.3847/1538-3881/153/2/77](https://doi.org/10.3847/1538-3881/153/2/77)
- Collins, K. A., Eastman, J. D., Beatty, T. G., et al. 2014, *AJ*, 147, 39, doi: [10.1088/0004-6256/147/2/39](https://doi.org/10.1088/0004-6256/147/2/39)
- Crane, J. D., Shtetman, S. A., & Butler, R. P. 2006, in *Proceedings of the SPIE*, Vol. 6269, doi: [10.1117/12.672339](https://doi.org/10.1117/12.672339)
- Crane, J. D., Shtetman, S. A., Butler, R. P., et al. 2010, in *Proceedings of the SPIE*, Vol. 7735, doi: [10.1117/12.857792](https://doi.org/10.1117/12.857792)
- Crane, J. D., Shtetman, S. A., Butler, R. P., Thompson, I. B., & Burley, G. S. 2008, in *Proceedings of the SPIE*, Vol. 7014, doi: [10.1117/12.789637](https://doi.org/10.1117/12.789637)

- Demory, B.-O., & Seager, S. 2011, *ApJS*, 197, 12, doi: [10.1088/0067-0049/197/1/12](https://doi.org/10.1088/0067-0049/197/1/12)
- Dobbs-Dixon, I., Lin, D. N. C., & Marling, R. A. 2004, *ApJ*, 610, 464, doi: [10.1086/421510](https://doi.org/10.1086/421510)
- Dong, S., Xie, J.-W., Zhou, J.-L., Zheng, Z., & Luo, A. 2018, *Proceedings of the National Academy of Science*, 115, 266, doi: [10.1073/pnas.1711406115](https://doi.org/10.1073/pnas.1711406115)
- Dotter, A. 2016, *ApJS*, 222, 8, doi: [10.3847/0067-0049/222/1/8](https://doi.org/10.3847/0067-0049/222/1/8)
- Eastman, J., Gaudi, B. S., & Agol, E. 2013, *PASP*, 125, 83, doi: [10.1086/669497](https://doi.org/10.1086/669497)
- Eastman, J., Siverd, R., & Gaudi, B. S. 2010, *PASP*, 122, 935, doi: [10.1086/655938](https://doi.org/10.1086/655938)
- Eastman, J. D., Rodriguez, J. E., Agol, E., et al. 2019, arXiv e-prints. <https://arxiv.org/abs/1907.09480>
- Enoch, B., Collier Cameron, A., & Horne, K. 2012, *A&A*, 540, A99, doi: [10.1051/0004-6361/201117317](https://doi.org/10.1051/0004-6361/201117317)
- Fausnaugh, M. M., Burke, C. J., Caldwell, D. A., et al. 2019a. https://archive.stsci.edu/missions/tess/doc/tess_drn/tess_sector_04_drn05_v04.pdf
- . 2019b. https://archive.stsci.edu/missions/tess/doc/tess_drn/tess_sector_05_drn07_v02.pdf
- Foreman-Mackey, D., Hogg, D. W., Lang, D., & Goodman, J. 2013, *PASP*, 125, 306, doi: [10.1086/670067](https://doi.org/10.1086/670067)
- Foreman-Mackey, D., Farr, W. M., Sinha, M., et al. 2019, emcee v3: A Python ensemble sampling toolkit for affine-invariant MCMC, v3.0.2, Zenodo, doi: [10.5281/zenodo.3543502](https://doi.org/10.5281/zenodo.3543502)
- Fortney, J. J., Marley, M. S., & Barnes, J. W. 2007, *ApJ*, 659, 1661, doi: [10.1086/512120](https://doi.org/10.1086/512120)
- Frandsen, S., & Lindberg, B. 1999, in *Astrophysics with the NOT*, ed. H. Karttunen & V. Pirola, 71
- Fulton, B., Blunt, S., Hurt, S., et al. 2019, *California-Planet-Search/radvel*, v1.3.2, Zenodo, doi: [10.5281/zenodo.3586003](https://doi.org/10.5281/zenodo.3586003)
- Fulton, B. J., Petigura, E. A., Blunt, S., & Sinukoff, E. 2018, *PASP*, 130, 044504, doi: [10.1088/1538-3873/aaaaa8](https://doi.org/10.1088/1538-3873/aaaaa8)
- Gaia Collaboration, Brown, A. G. A., Vallenari, A., et al. 2018, *A&A*, 616, A1, doi: [10.1051/0004-6361/201833051](https://doi.org/10.1051/0004-6361/201833051)
- Gandolfi, D., Barragán, O., Hatzes, A. P., et al. 2017, *AJ*, 154, 123, doi: [10.3847/1538-3881/aa832a](https://doi.org/10.3847/1538-3881/aa832a)
- Goldreich, P., & Soter, S. 1966, *Icarus*, 5, 375, doi: [10.1016/0019-1035\(66\)90051-0](https://doi.org/10.1016/0019-1035(66)90051-0)
- Goodman, J., & Weare, J. 2010, *Communications in Applied Mathematics and Computational Science*, 5, 65, doi: [10.2140/camcos.2010.5.65](https://doi.org/10.2140/camcos.2010.5.65)
- Guerrero, N., Seager, S., Huang, C. X., et al. submitted, The TESS Objects of Interest Catalog from the TESS Prime Mission
- Harris, C. R., Millman, K. J., van der Walt, S. J., et al. 2020, *Nature*, 585, 357, doi: [10.1038/s41586-020-2649-2](https://doi.org/10.1038/s41586-020-2649-2)
- Hartman, J. D., & Bakos, G. A. 2016, *A&C*, 17, 1, doi: [10.1016/j.ascom.2016.05.006](https://doi.org/10.1016/j.ascom.2016.05.006)
- Hartman, J. D., Bakos, G. Á., Bhatti, W., et al. 2016, *AJ*, 152, 182, doi: [10.3847/0004-6256/152/6/182](https://doi.org/10.3847/0004-6256/152/6/182)
- Hatzes, A. P., & Rauer, H. 2015, *ApJL*, 810, L25, doi: [10.1088/2041-8205/810/2/L25](https://doi.org/10.1088/2041-8205/810/2/L25)
- Huang, X., Sha, L., & Vanderburg, A. 2019, in *AAS Meeting Abstracts*, Vol. 233, 467.08
- Huber, D., Bryson, S. T., Haas, M. R., et al. 2016, *ApJS*, 224, 2, doi: [10.3847/0067-0049/224/1/2](https://doi.org/10.3847/0067-0049/224/1/2)
- Huber, D., Chaplin, W. J., Chontos, A., et al. 2019, *AJ*, 157, 245, doi: [10.3847/1538-3881/ab1488](https://doi.org/10.3847/1538-3881/ab1488)
- Hunter, J. D. 2007, *Computing in Science Engineering*, 9, 90, doi: [10.1109/MCSE.2007.55](https://doi.org/10.1109/MCSE.2007.55)
- Jenkins, J. M., Twicken, J. D., McCauliff, S., et al. 2016, in *Proc. SPIE*, Vol. 9913, *Software and Cyberinfrastructure for Astronomy IV*, 99133E, doi: [10.1117/12.2233418](https://doi.org/10.1117/12.2233418)
- Jensen, E. 2013, Tapir: A web interface for transit/eclipse observability. <http://ascl.net/1306.007>
- K2 Science Office. 2020. <https://keplerscience.arc.nasa.gov/k2-data-release-notes.html#k2-campaign-19>
- Kaufer, A., Stahl, O., Tubbesing, S., et al. 1999, *The Messenger*, 95, 8. <http://articles.adsabs.harvard.edu/full/1999Msngr..95....8K>
- Kipping, D. M. 2013, *MNRAS*, 435, 2152, doi: [10.1093/mnras/stt1435](https://doi.org/10.1093/mnras/stt1435)
- Kovács, G., Bakos, G., & Noyes, R. W. 2005, *MNRAS*, 356, 557, doi: [10.1111/j.1365-2966.2004.08479.x](https://doi.org/10.1111/j.1365-2966.2004.08479.x)
- Kovács, G., Zucker, S., & Mazeh, T. 2002, *A&A*, 391, 369, doi: [10.1051/0004-6361:20020802](https://doi.org/10.1051/0004-6361:20020802)
- Kreidberg, L. 2015, *PASP*, 127, 1161, doi: [10.1086/683602](https://doi.org/10.1086/683602)
- Lainey, V., Jacobson, R. A., Tajeddine, R., et al. 2017, *Icarus*, 281, 286, doi: [10.1016/j.icarus.2016.07.014](https://doi.org/10.1016/j.icarus.2016.07.014)
- Lenzen, R., Hartung, M., Brandner, W., et al. 2003, in *Proceedings of the SPIE*, Vol. 4841 (SPIE), 944–952, doi: [10.1117/12.460044](https://doi.org/10.1117/12.460044)
- Li, J., Caldwell, D. A., Jenkins, J. M., et al. 2018, in *American Astronomical Society Meeting Abstracts*, Vol. 232, 120.03
- Lucy, L. B., & Sweeney, M. A. 1971, *AJ*, 76, 544, doi: [10.1086/111159](https://doi.org/10.1086/111159)
- Mayor, M., Pepe, F., Queloz, D., et al. 2003, *The Messenger*, 114, 20. <http://www.eso.org/sci/publications/messenger/archive/no.114-dec03/messenger-no114-20-24.pdf>
- Miller, N., & Fortney, J. J. 2011, *ApJL*, 736, L29, doi: [10.1088/2041-8205/736/2/L29](https://doi.org/10.1088/2041-8205/736/2/L29)
- Morton, T. D. 2015, isochrones: Stellar model grid package. <http://ascl.net/1503.010>
- Mulders, G. D., Pascucci, I., Apai, D., Frasca, A., & Molenda-Žakowicz, J. 2016, *AJ*, 152, 187, doi: [10.3847/0004-6256/152/6/187](https://doi.org/10.3847/0004-6256/152/6/187)
- Pandas Development Team. 2020, pandas-dev/pandas: Pandas 1.0.3, v1.0.3, Zenodo, doi: [10.5281/zenodo.3715232](https://doi.org/10.5281/zenodo.3715232)

- Pedregosa, F., Varoquaux, G., Gramfort, A., et al. 2011, *Journal of Machine Learning Research*, 12, 2825
- Pepe, F., Mayor, M., Rupprecht, G., et al. 2002, *The Messenger*, 110, 9.
<http://articles.adsabs.harvard.edu/full/2002Msng.110....9P>
- Petigura, E. A., Sinukoff, E., Lopez, E. D., et al. 2017, *AJ*, 153, 142, doi: [10.3847/1538-3881/aa5ea5](https://doi.org/10.3847/1538-3881/aa5ea5)
- Petigura, E. A., Marcy, G. W., Winn, J. N., et al. 2018, *AJ*, 155, 89, doi: [10.3847/1538-3881/aaa54c](https://doi.org/10.3847/1538-3881/aaa54c)
- Prša, A., Harmanec, P., Torres, G., et al. 2016, *AJ*, 152, 41, doi: [10.3847/0004-6256/152/2/41](https://doi.org/10.3847/0004-6256/152/2/41)
- Queloz, D., Mayor, M., Udry, S., et al. 2001, *The Messenger*, 105, 1. <http://articles.adsabs.harvard.edu/full/2001Msng.105....1Q>
- Ricker, G. R., Winn, J. N., Vanderspek, R., et al. 2015, *Journal of Astronomical Telescopes, Instruments, and Systems*, 1, 014003, doi: [10.1117/1.JATIS.1.1.014003](https://doi.org/10.1117/1.JATIS.1.1.014003)
- Rousset, G., Lacombe, F., Puget, P., et al. 2003, in *Proc. SPIE*, Vol. 4839, 140–149, doi: [10.1117/12.459332](https://doi.org/10.1117/12.459332)
- Schlegel, D. J., Finkbeiner, D. P., & Davis, M. 1998, *ApJ*, 500, 525, doi: [10.1086/305772](https://doi.org/10.1086/305772)
- Scott, N. J., Howell, S. B., Horch, E. P., & Everett, M. E. 2018, *PASP*, 130, 054502, doi: [10.1088/1538-3873/aab484](https://doi.org/10.1088/1538-3873/aab484)
- Stassun, K. G., Collins, K. A., & Gaudi, B. S. 2017, *AJ*, 153, 136, doi: [10.3847/1538-3881/aa5df3](https://doi.org/10.3847/1538-3881/aa5df3)
- Stassun, K. G., Corsaro, E., Pepper, J. A., & Gaudi, B. S. 2018, *AJ*, 155, 22, doi: [10.3847/1538-3881/aa998a](https://doi.org/10.3847/1538-3881/aa998a)
- Stassun, K. G., & Torres, G. 2016, *AJ*, 152, 180, doi: [10.3847/0004-6256/152/6/180](https://doi.org/10.3847/0004-6256/152/6/180)
- . 2018, *ApJ*, 862, 61, doi: [10.3847/1538-4357/aaca4c](https://doi.org/10.3847/1538-4357/aaca4c)
- Stassun, K. G., Oelkers, R. J., Paegert, M., et al. 2019, *AJ*, 158, 138, doi: [10.3847/1538-3881/ab3467](https://doi.org/10.3847/1538-3881/ab3467)
- Szentgyorgyi, A. 2004.
<http://www.sao.arizona.edu/FLWO/60/TRES/TRESdesign.pdf>
- Tan, T.-G. n.d. <http://pestobservatory.com/the-pest-pipeline/>
- Telting, J. H., Avila, G., Buchhave, L., et al. 2014, *Astronomische Nachrichten*, 335, 41, doi: [10.1002/asna.201312007](https://doi.org/10.1002/asna.201312007)
- Tokovinin, A. 2018, *PASP*, 130, 035002, doi: [10.1088/1538-3873/aaa7d9](https://doi.org/10.1088/1538-3873/aaa7d9)
- Tokovinin, A., Fischer, D. A., Bonati, M., et al. 2013, *PASP*, 125, 1336, doi: [10.1086/674012](https://doi.org/10.1086/674012)
- Twicken, J. D., Catanzarite, J. H., Clarke, B. D., et al. 2018, *PASP*, 130, 064502, doi: [10.1088/1538-3873/aab694](https://doi.org/10.1088/1538-3873/aab694)
- Vanderburg, A., & Johnson, J. A. 2014, *PASP*, 126, 948, doi: [10.1086/678764](https://doi.org/10.1086/678764)
- Vanderburg, A., Latham, D. W., Buchhave, L. A., et al. 2016, *ApJS*, 222, 14, doi: [10.3847/0067-0049/222/1/14](https://doi.org/10.3847/0067-0049/222/1/14)
- Virtanen, P., Gommers, R., Oliphant, T. E., et al. 2020, *Nature Methods*, 17, 261, doi: [10.1038/s41592-019-0686-2](https://doi.org/10.1038/s41592-019-0686-2)
- Wakeford, H. R., Sing, D. K., Deming, D., et al. 2018, *AJ*, 155, 29, doi: [10.3847/1538-3881/aa9e4e](https://doi.org/10.3847/1538-3881/aa9e4e)
- Winn, J. N., Holman, M. J., Torres, G., et al. 2008, *ApJ*, 683, 1076, doi: [10.1086/589737](https://doi.org/10.1086/589737)
- Ziegler, C., Tokovinin, A., Briceño, C., et al. 2020, *AJ*, 159, 19, doi: [10.3847/1538-3881/ab55e9](https://doi.org/10.3847/1538-3881/ab55e9)